Coordinated Ground#Based and Space#Borne Observations of Ionospheric Response to the Annular Solar Eclipse on 26 December 2019

1 # Coordinated ground-based and space-borne
2 # observations of ionospheric response to the annular
3 # solar eclipse on 26 December 2019

4 **Ercha Aa[1,2], Shun-Rong Zhang[1], Philip J. Erickson[1], Larisa P. Goncharenko[1],**
5 **Anthea J. Coster[1], Olusegun F. Jonah[1], Jiuhou Lei[3,4,5], Fuqing Huang[3,4,5],**
6 **Tong Dang[3,4,5], and Lei Liu[6]**

7 [1]Haystack Observatory, Massachusetts Institute of Technology, Westford, MA, USA.
8 [2]National Space Science Center, Chinese Academy of Sciences, Beijing, China.
9 [3]CAS Key Laboratory of Geospace Environment, School of Earth and Space Sciences, University of
10 Science and Technology of China, Hefei, China.
11 [4]Mengcheng National Geophysical Observatory, University of Science and Technology of China, Hefei,
12 China.
13 [5]Chinese Academy of Sciences Center for Excellence in Comparative Planetology, University of Science
14 and Technology of China, Hefei, China.
15 [6]School of Geodesy and Geomatics, Wuhan University, Wuhan, China.

16 **Key Points:**

17 - EEJ was weakened substantially during morning eclipse, contributing to a signif-
18   icant TEC depletion and prolonged recovery period therein
19 - EIA crest exhibited 20–40% enhancement and 3–4° poleward shifting, likely trig-
20   gered by modified neutral wind and electrodynamics patterns
21 - Topside Ne showed considerable altitudinal difference, exhibiting ∼30% reduction
22   at 500 km and ∼30% enhancements with Te reduction of 300–500 K at 850 km

Corresponding author: E. Aa, aercha@mit.edu

Abstract

This paper studies the ionosphere's response to the annular solar eclipse on 26 December 2019, utilizing the following ground-based and space-borne measurements: Global Navigation Satellite System (GNSS) total electron content (TEC) data, spectral radiance data from the Sentinel-5P satellite, in situ electron density and/or temperature measurements from DMSP and Swarm satellites, and local magnetometer data. Analysis concentrated on ionospheric effects over low-latitude regions with respect to obscuration, local time, latitude, and altitude. The main results are as follows: (1) a local TEC reduction of ∼4–6 TECU (30–50%) was identified along the annular eclipse path, with larger depletion and longer recovery periods in the morning eclipse compared to midday. (2) The equatorial electrojet current was significantly weakened when the eclipse trajectory crossed the magnetic equator in the morning (India) sector, which contributed to large and prolonged TEC depletion therein. (3) At midday, equatorial ionization anomaly exhibited enhancements of 20–40% as well as poleward shifting of 3–4°, likely triggered by modified neutral wind and electrodynamics patterns. (4) The behavior of equatorial ionospheric electron density showed considerable altitudinal differences in the topside, exhibiting ∼30% reduction around 500 km and ∼30% enhancement with 300–500 K Te reduction around 850 km, before the arrival of maximum eclipse. This may have been caused by the enhanced eastward electric field and equatorward neutral wind, and other possible factors are also discussed.

1 Introduction

A solar eclipse is one of the most stunning celestial phenomena, and has provided unique opportunities to study many fundamental ionospheric processes due to the transient obscuration of solar radiation (Rishbeth, 1968). For the past decades, solar eclipse effects on the ionosphere have been extensively investigated using different instruments and measurements, such as ionograms recorded by ionosondes (Evans, 1965; J. Liu et al., 1998; G. Chen et al., 2011, 2013; Reinisch et al., 2018), high-frequency Doppler measurements (Cheng et al., 1992; Jakowski et al., 2008), plasma density and temperature measurements from incoherent scatter radars (Salah et al., 1986; MacPherson et al., 2000; Momani et al., 2010; L. P. Goncharenko et al., 2018), total electron content (TEC) observations from ground-based Global Navigation Satellite Systems (GNSS) (Afraimovich et al., 1998; Ding et al., 2010; Hoque et al., 2016; Coster et al., 2017; Zhang et al., 2017; Cherniak & Zakharenkova, 2018), as well as in situ measurements from low-Earth orbiting satellites (Cherniak & Zakharenkova, 2018; Yau et al., 2018; Hussien et al., 2020). Moreover, a number of studies have explored the global ionosphere-thermosphere responses to the solar eclipse using numerical simulations (e.g., Müller-Wodarg et al., 1998; Le et al., 2008a, 2008b; Huba & Drob, 2017; Dang et al., 2018; Lei, Dang, et al., 2018; Wu et al., 2018; Wang et al., 2019; Dang et al., 2020).

The ionospheric response to a solar eclipse manifests in various aspects. These include (1) A local decrease of ionization during the eclipse: An average reduction of 20–40% for ionospheric TEC and electron density at bottomside F-layer can be observed along the eclipse path due to reduced solar extreme ultraviolet (EUV) flux, and the deepest depletion usually occurs shortly (several to tens of minutes) after the maximum obscuration (e.g., Afraimovich et al., 1998; Jakowski et al., 2008; Ding et al., 2010; Momani et al., 2010; Coster et al., 2017; Cherniak & Zakharenkova, 2018). (2) A cooling in plasma temperature: There can be a 100- to 1000-K cooling in electron temperature due to reduced photo-electron heating via solar EUV, and the ion temperature often exhibits ∼100 K decrease due to enhanced thermospheric cooling and smaller heat transfer from electrons via Coulomb collisions (e.g., MacPherson et al., 2000; Momani et al., 2010; L. P. Goncharenko et al., 2018). (3) Complex electron density behavior in the topside ionosphere: The significant drop of electron and ion temperatures can reduce the equilibrium plasma scale height, thus enhancing downward ion diffusion (e.g. Evans, 1965; Jakowski et al.,

2008; Huba & Drob, 2017). This dynamic response is particularly complex because the competing effects of diffusion, photo-chemistry, neutral wind, and electric field transportation can make the net electron density above the F2 peak decrease, remain unchanged, or even slightly increase during the eclipse (e.g., Wu et al., 2018; Wang et al., 2019). (4) Eclipse-induced gravity waves and bow waves: Sudden atmospheric cooling and heating associated with eclipse can excite internal gravity waves that propagate upward to thermosphere heights (e.g., Chimonas, 1970; C. Y. Lin et al., 2018; Nayak & Yiğit, 2018; Dang et al., 2018), and the supersonic movement of lunar shadow can induce atmospheric bow waves (e.g., J. Y. Liu et al., 2011; Zhang et al., 2017; Sun et al., 2018).

Recently, the Great American Eclipse, which passed through the continental United States from northwest to southeast on 21 August 2017, offered a rare opportunity to study the midlatitude ionosphere and thermosphere response in detail with unprecedented dense observational instruments. Besides the above-mentioned eclipse effects, a number of interesting findings were reported as well, such as large-scale TEC and NmF2 depletion for more than 50% (e.g., Coster et al., 2017; Cherniak & Zakharenkova, 2018; Reinisch et al., 2018), travelling ionospheric disturbances and thermospheric wave (e.g., Zhang et al., 2017; Mrak et al., 2018; Nayak & Yiğit, 2018; Harding et al., 2018; Pradipta et al., 2018; Eisenbeis et al., 2019), enhanced and long-lasting posteclipse response (e.g., Lei, Dang, et al., 2018; Wu et al., 2018), topside ionosphere composition change and interhemispheric ion flows (e.g., Yau et al., 2018; Perry et al., 2019), etc.

Although significant progress has been obtained through previous eclipse studies, our knowledge of the ionospheric response to equatorial eclipse event remains incomplete, and some important issues need to be further investigated. For example, how does the equatorial dynamo change due to the impact of a solar eclipse? In particular, the electrodynamics of the ionospheric fountain mechanism could be complicated by solar eclipse due to conductivity variations, since the magnitude of eclipse-associated TEC depletion at equatorial latitudes can reach more than 40%, larger than those at mid-latitudes (Huang et al., 1999; Tsai & Liu, 1999; Dear et al., 2020). Moreover, to what degree is the equatorial ionization anomaly (EIA) modified by a solar eclipse? Previous reports indicate that an eclipse may trigger a strong oscillation in the zonal electric field and neutral wind circulation pattern, causing a pronounced reduction or even enhancement in the equatorial ionization anomaly (EIA) zone (e.g., Tomás et al., 2008; Choudhary et al., 2011; St. -Maurice et al., 2011; C.-H. Chen et al., 2019; Dang et al., 2020). The dominant mechanism for this effect is still under debate. For these reasons, it is of great importance to further study these eclipse associated characteristics and to understand the role of different mechanisms in generating large-scale changes in the equatorial ionosphere under eclipse conditions.

On 26 December 2019 between 04:00–07:00 UT, an annular solar eclipse traveled across the equatorial region over south Asia, providing a good opportunity to investigate the eclipse induced dynamo effect at low latitudes that may modify EIA intensity and location. In this paper, we present coordinated ground-based and space-borne observations of this eclipse event by using multi-instrument measurements: ground-based GNSS TEC data, Sentinel-5P satellite ultraviolet-visible spectral data, in situ measurements from both the Swarm constellation and the Defense Meteorological Satellite Program (DMSP) constellation, and local equatorial magnetometer measurements. The rest of the paper is organized as follows: the data set is described in section 2. Results and discussion of equatorial eclipse effects and mechanisms are given in section 3 and section 4, respectively. The conclusions are presented in section 5.

2 Data Description

GNSS TEC data are produced and provided through the Madrigal distributed data system developed at the Massachusetts Institute of Technology's Haystack Observatory

by using dense networks of worldwide GNSS receivers (Rideout & Coster, 2006; Vierinen et al., 2016). For this study, part of the GNSS available measurements were also accessed from the Crustal Movement Observation Network of China (CMONOC) (e.g., Aa, Huang, Liu, et al., 2015; Aa, Huang, Yu, et al., 2015; L. Liu et al., 2020). The gridded TEC maps were constructed by binning all GNSS-derived TEC values into 1° (latitude) × 1° (longitude) cells at 5 min interval. We also used TEC data from Beidou geostationary orbit (GEO) satellites in the Asian sector. Beidou GEO satellites have fixed ionospheric pierce points and can give more reliable observations of TEC as compared with non-GEO satellites (Hu et al., 2017; Lei, Huang, et al., 2018). For more details on the network description and TEC derivation, readers may refer to the above-mentioned references.

The Sentinel-5 Precursor (S5P) satellite mission for atmospheric monitoring was launched on 13 October 2017 and is operating in a Sun-synchronous orbit at 824 km with an inclination of 98° and overpass time of 13:30 local solar time. The sole instrument on Sentinel-5P is the TROPOspheric Monitoring Instrument (TROPOMI) that measures the radiance and composition variation of the lower atmosphere. TROPOMI is a nadir-viewing push-broom imaging spectrometer with 108° field-of-view, covering wavelengths of ultraviolet-visible (270–495 nm), near-infrared (675–775 nm), and shortwave infrared (2305–2385 nm) (Veefkind et al., 2012). This paper uses spectral measurements in the ultraviolet-visible band to show eclipse-induced radiance variations in the lower atmosphere. These measurements were subsequently used in a qualitative sense to estimate radiance change in the ionosphere. (No measurements of eclipse-induced EUV variation were available for this eclipse event.)

Additionally, in situ electron density and up-looking TEC measurements from the Swarm B satellite at ∼500 km, as well as electron density and temperature data from the DMSP F16 sun-synchronous satellite at ∼850 km, are used to analyze ionospheric response to the solar eclipse. Magnetometer data at the Alibag (18.62°N, 72.87°E) and Kototabang (0.2°S, 100.32°E) stations were also utilized to study eclipse-induced local magnetic field variations.

3 Results

Figure 1 shows the temporal variation of F10.7, Kp, interplanetary magnetic field (IMF) Bz, interplanetary electric field, and Dst indices in December 2019. The gray areas show the interval of solar eclipse on 26 December. During this period, the solar activity maintained at very low level with F10.7 ranging from 67 to 70 sfu and no considerable flares from visible solar disk. The geomagnetic activity reached active levels (Kp=4) during 18–19 December due to a recurrent coronal hole high speed stream, and remained at quiet to unsettled levels for the rest of the month. The reference value for evaluating eclipse-induced TEC variation need to be carefully selected. In order to minimize the effects of magnetosphere driving forces for strong ionospheric variation, we here use mean values of 10 quiet-time (Kp≤2) days that not too far away from the eclipse day as the reference: December 16, 22-25, and 27-31.

3.1 Ground-based Observations

Figure 2a shows the regional distribution of GNSS receivers (70°E–140°E, 20°S–30°N) used in this study with the superimposed annular solar eclipse path as well as the 80%, 60%, and 40% obscuration lines. Figure 2b displays a gridded vertical TEC map at 05:30 UT on 26 December 2019. The corresponding maximum eclipse location and different obscuration lines are also shown. Data coverage over the EIA region that around ±15° MLAT, especially over the northern crest, is considered sufficient for this study. We first consider three equatorial GNSS receivers that are located closest to the annular eclipse path: IISC (12.9°N, 77.6°E, MLAT=6.5°), SGOC (6.9°N, 79.9°E, MLAT=-
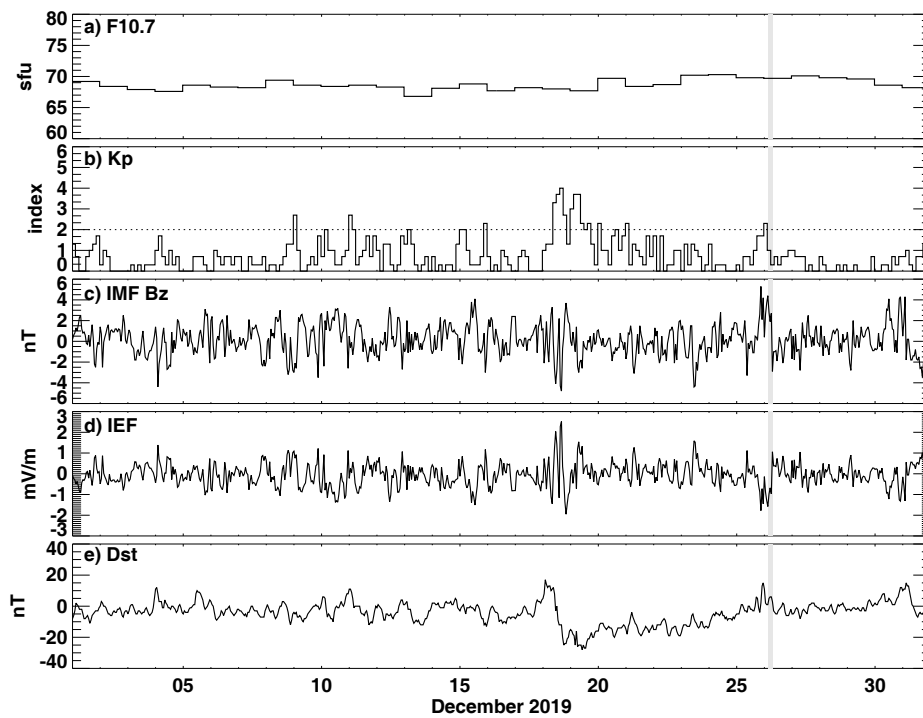
Figure 1. (a–e) The temporal variation of F10.7, Kp, IMF Bz, Interplanetary electric field, and Dst indices in December 2019. The vertical gray areas indicate the solar eclipse interval at 03–07 UT on 26 December 2019.
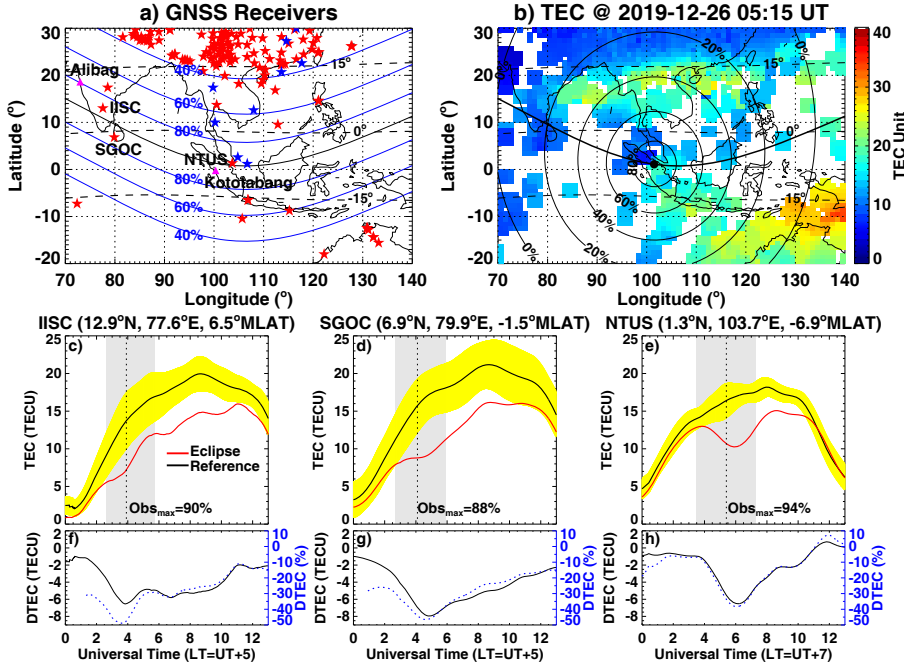
Figure 2. (a) Geographic location of Asian sector GNSS receivers used in this study are plotted (star) with Beidou GEO TEC receivers being colored by blue. The annular solar eclipse path (black curve) as well as the 80%, 60%, and 40% obscuration lines (blue curves) are plotted. The geomagnetic equator and $\pm 15°$ are plotted with a dashed line. Three GNSS receivers (IISC, SGOC, and NTUS) and two magnetometers at Alibag and Kototabang (magenta triangle) were located nearby the annular eclipse path as marked. (b) Gridded TEC map with the location of maximum eclipse obscuration (dot) and different obscuration percentages (black ellipsoids) at 05:15 UT on 26 December 2019. (c–e) TEC temporal variations during the eclipse day (red) compared to reference days (black) for IISC, SGOC, and NTUS receivers. The one-σ deviations are marked with yellow error bars. The shaded region shows the duration of the eclipse. The maximum obscuration percentage was recorded with its time being marked by a vertical dotted line. (f–h) Differential TEC (solid black) and percentage TEC (dashed blue) variations for IISC, SGOC, and NTUS calculated with respect to averaged background reference values.

176   1.5°), and NTUS (1.3°N, 103.7°E, MLAT=-6.9°). Figures 2c–2e show TEC variations
177   during the eclipse day (Dec 26) along with reference non-eclipse values (mean values of
178   ten days as mentioned above) for those three receivers. Figures 2f–2h show the corre-
179   sponding differential TEC variations in TEC units (TECU = 10^{16} el/m^2) and also plot
180   variation percentage with respect to the averaged value on reference days.

181   For all three receivers, TEC values showed a clear reduction during the eclipse. Specif-
182   ically, there was a slight difference in responses between these receivers with somewhat
183   dependence on the local time of the eclipse. For IISC and SGOC, the eclipse started in
184   the morning, only shortly after local sunrise around December solstice. At this time, the
185   ionosphere was still forming due to EUV illumination, and therefore photo-chemical pro-
186   cesses assumed a more dominant role than transportation processes (Rishbeth et al., 1995).
187   At the equator, eclipse-induced ionization deficiency was further exacerbated by plasma
188   loss via the equatorial fountain effect. Taken as a whole, these factors collectively cre-

–6–

ated a considerable TEC depletion: -6.5 TECU (-49.1%) at IISC and -7.9 TECU (-46.9%) at SGOC. The time delay between the maximum obscuration and largest TEC depletion was almost negligible at IISC and was ~30 min at SGOC. Both stations exhibited an extended recovery time of ~4–6 hours after local eclipse end. By contrast, at NTUS, the moon shadow transited the ionosphere around local noon, when the daytime ionosphere was well-established and plasma transport process were already dominant over production process. Thus, when compared with the morning time eclipse, the TEC observed at NTUS showed a smaller depletion peak of -6.4 TECU (-38.2%) with the post-eclipse recovery time being around 3–4 hours.

However, it is worth noting that normal ionospheric day-to-day variation could be very significant especially during the eclipse day: all three TEC curves showed lower overall level compared with reference values, exhibiting somewhat earlier deviations from background curve before local eclipse start as well as prolonged post-eclipse recovery. This could also make contributions to the observed local time differences between stations. Specifically, the reference days were selected to be under geomagnetically quiet conditions (Kp≤2). For the eclipse day, however, Kp reached 2+ in the 00-03 UT, likely triggered by a quick northward turning of IMF Bz associated with negative excursion of interplanetary electric field at the end of 25 December as can be seen in Figure 1c and 1d. This could cause a temporarily dominant shielding electric field effects that partially penetrated into the low latitude, which presumes occurrence of westward (eastward) zonal electric field on the dayside (nightside) (Kikuchi et al., 2008). This might lead to the earlier reductions of TEC curves during the eclipse day as mentioned above. In addition, low-latitude ionosphere can also be strongly affected by stratospheric disturbances, in particular in December-February season during the times of sudden stratospheric warming (L. Goncharenko et al., 2020). In the end of December 2019, stratospheric temperature and zonal winds were not disturbed and remained close to their multi-year mean values, indicating that meteorological driving forcing is not expected to generate strong ionospheric variations. Moreover, for other midlatitude eclipse events, studies have reported that TEC/NmF2 depletions were usually larger around midday as compared to morning times (e.g., Le et al., 2008b; Ding et al., 2010; Cherniak & Zakharenkova, 2018). These trends are opposite to our results for this equatorial eclipse, raising the question that to what degree this "abnormal" local time effect can be attributed to solar eclipse influences. Further investigation of this question is provided in the discussion section.

To further reveal the temporal-spatial evolution of eclipse-induced ionospheric variations, Figure 3 and Figure 4 show the absolute TEC and differential TEC maps (calculated with respect to averaged values for reference days) at different time steps during 04–08 UT on eclipse day. The differential TEC results show a long-lasting depletion over the Indian sector, similar to the sunrise local time effect mentioned above. Moreover, some general characteristics of ionospheric response can be summarized as: (1) The average TEC reduction along the annular eclipse path was ~4–6 TECU (~30–50%); (2) Most of the significant TEC depletion occurred interior to the 60% obscuration zone; (3) The time lag between maximum TEC depletion and maximum eclipse obscuration was ~30–60 min over 100°–120°E.

Another notable response feature was the presence of pronounced TEC enhancements over the northern and southern crests of the midday EIA region between 100°–130°E. The TEC relative increase appeared before the arrival of maximum obscuration with a magnitude of 1–2 TECU, but this increase was further amplified during the eclipse, reaching 4–7 TECU (~20–40%). This early formation and intensification of EIA before eclipse arrival was also reported by some studies (Huang et al., 1999; Tsai & Liu, 1999; C.-H. Chen et al., 2019), but its triggering mechanism is still debated. In particular, ionospheric day-to-day variability should play a role, and Huang et al. (1999) and Tsai and Liu (1999) concluded in fact that pre-eclipse increase of TEC was due to the location difference of the EIA crest between the eclipse and reference days, implying that day-

–7–
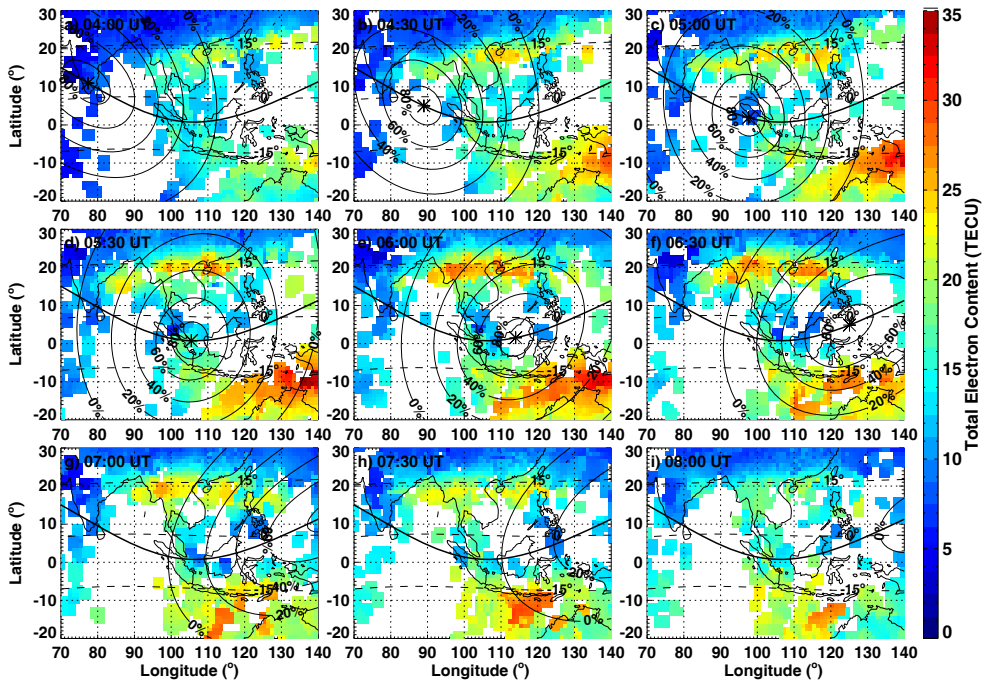
Figure 3. (a–i) Two-dimensional gridded TEC maps with 30-min interval during 04:00–08:00 UT on 26 December 2019. The thick line shows the annular eclipse path, and the asterisk marks the maximum eclipse location for current time step. Different solar obscuration zones (80%, 60%, 40%, 20%, and 0%) as well as geomagnetic equator and ±15° are also shown.
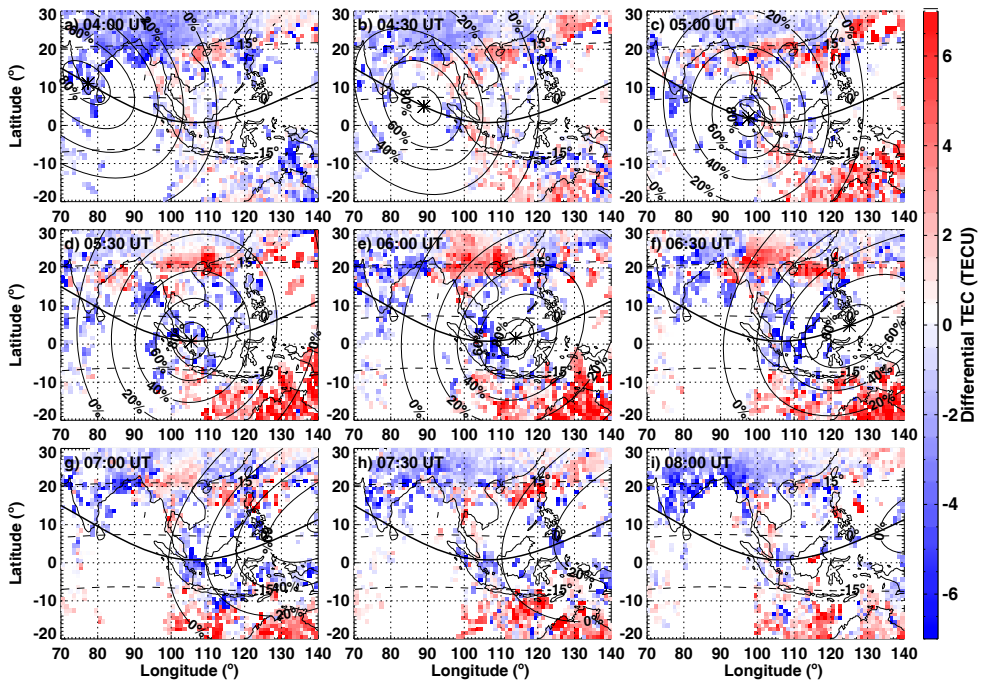
**Figure 4.** The same as Figure 3, but for the differential TEC maps.
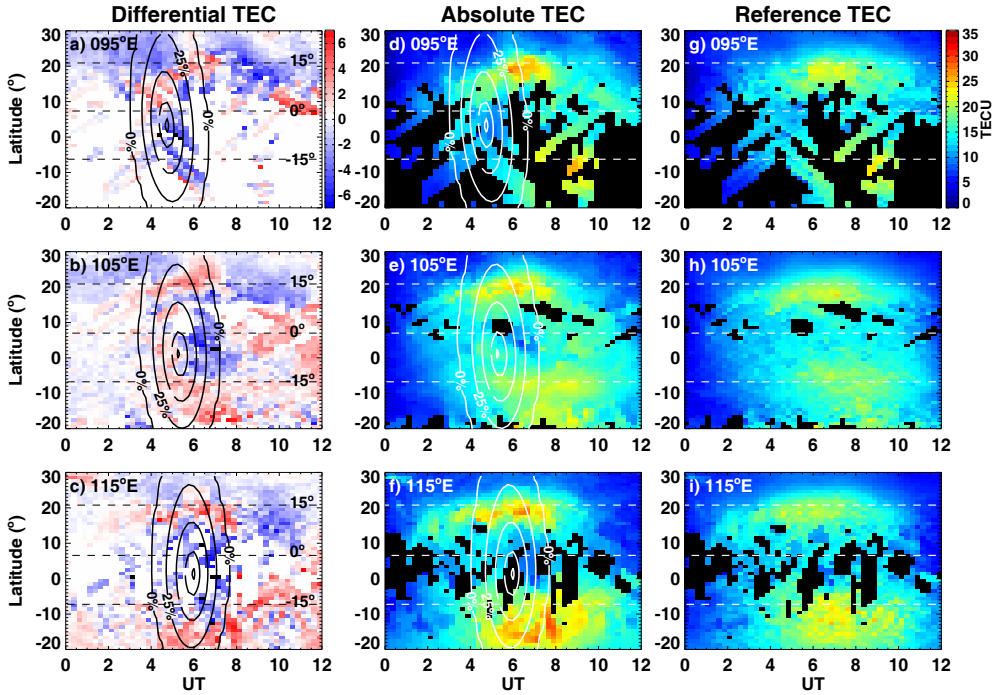
Figure 5. The differential (a–c), absolute (d–f), and reference (g–i) TEC values as a function of latitude and time along different longitudes (95°E, 105°E, and 115°E). The black pixel in absolute TEC is due to data gaps. Different solar obscuration degree (90%, 75%, 50%, 25%, and 0%) as well as geomagnetic equator and ±15° are also shown.

to-day variability can dominate eclipse influences. This is plausible even for our event, as EIA is known to be highly variable on a day-to-day basis (Basu et al., 2009). However, C.-H. Chen et al. (2019) indicated by contrast that this mechanism itself is not enough, and that eclipse-induced variations in electrodynamic forcing through electric field changes might also play a role. Dang et al. (2020) and Jonah et al. (2020) also pointed out that eclipse-induced neutral wind changes can also enhance the EIA. For current eclipse event, comparison of DTEC results at 4 UT (Figure 4a), 6 UT (Figure 4e), and 8 UT (Figure 4i) indicates that an earlier weak TEC enhancement around EIA crest was present but was effectively amplified during the eclipse. Thus, we conclude it is likely that a combination of eclipse-induced electric field and neutral wind changes, with some contribution by day-to-day ionospheric variability, collectively played a role in generating this enhanced and prolonged EIA crest. Quantifying the relative contribution of these multiple influences is beyond the scope of this study, but should be addressed in the future using numerical simulation and/or model-data assimilative studies.

To further demonstrate EIA variations during the midday eclipse, Figure 5 shows a keogram plot of meridional slices of differential TEC and absolute TEC (eclipse and reference days) as a function of time at three different longitudes. At 95°E longitude, the EIA northern crest showed a clear enhancement during the eclipse. At 105°E and 115°E, the above-mentioned earlier appearance and ascension of EIA before the eclipse can be seen especially for the northern crest. However, through comparing absolute TEC during eclipse day and reference days, it can be seen that this early ascension of EIA crests had noticeable enhancements of 4–7 TECU that occurred primarily during the eclipse, followed by a TEC reduction of 4–6 TECU in the equatorial obscuration zone, indicat-

–9–

265 ing possible contribution from the eclipse. Moreover, the EIA crests had a similar local
266 time variation for eclipse and reference days, though the crest peak location exhibited
267 a slight poleward shifting of ∼3° on the eclipse day (e.g., comparing Figures 5e and 5h,
268 5f and 5i). However, it is hard to ascertain to what extent such a modest movement can
269 be ascribed to eclipse since the day-to-day variation of EIA location could also make a
270 contribution, and future numerical simulations are needed to further address this issue.

271 In addition, Figure 6 plots the temporal variation of Beidou GEO TEC at nine re-
272 ceivers located approximately within the same meridional sector (100°–120°E) affected
273 by the midday eclipse. In particular, the eclipse-induced TEC bite-out phenomenon can
274 be clearly seen at equatorial receiver locations (Figures 6f–6i). We also note that near
275 the EIA crest region (Figure 6c and 6d), there are large day-to-day variations: the TEC
276 on the eclipse day had generally higher values than the two previous days, but was smaller
277 than or comparable to TEC values on Dec 23 and 27. In addition, the daily TEC peak
278 on eclipse day occurred after the eclipse maximum. By contrast, for the non-eclipse days,
279 the daily peak usually occurred at an earlier local time, before values associated with
280 eclipse maximum time. Taken Figures 5 and 6 as a whole, these results collectively in-
281 dicate to some extent, that the eclipse provided additional contributions to EIA crest
282 enhancement besides day-to-day variation. We will further analyze the possible mech-
283 anisms of eclipse-induced EIA crest enhancement and widening phenomena in the dis-
284 cussion section.
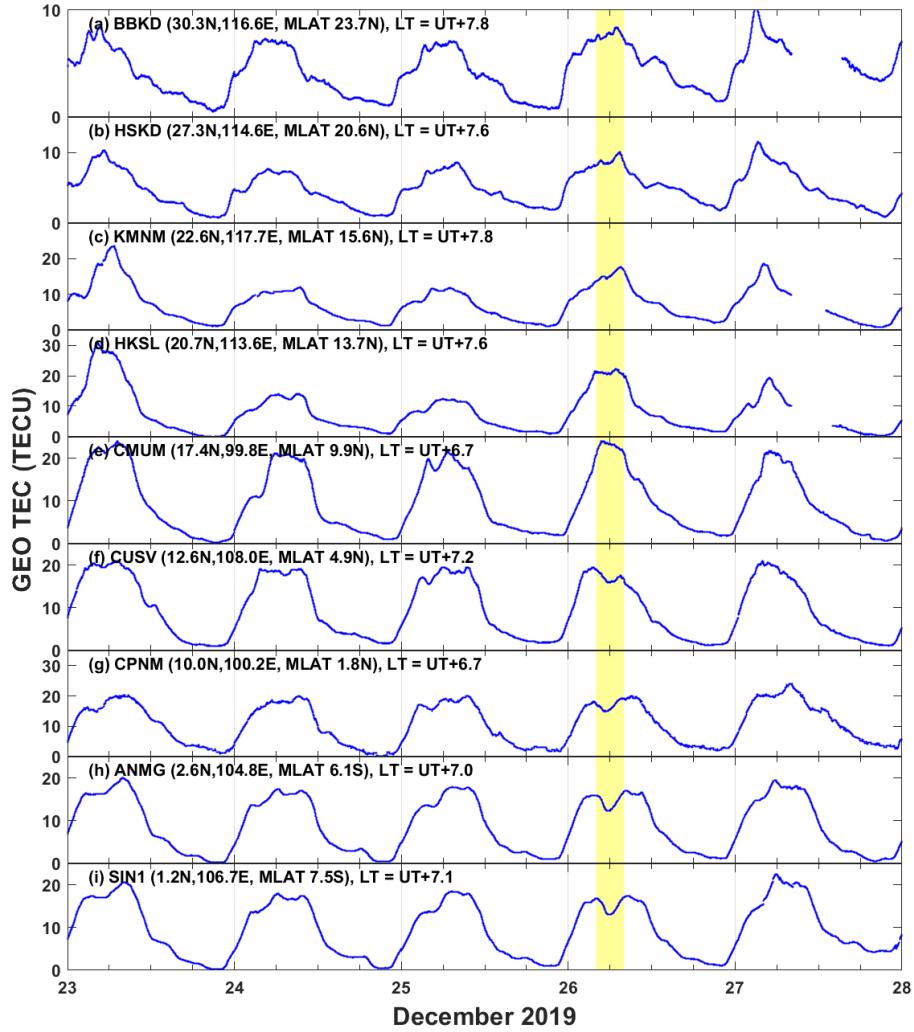
Figure 6. Beidou GEO TEC variation during 23–28 December 2019 at nine receivers that locate approximately within the same longitudinal sector (100°–120°E). The eclipse interval is marked by yellow shadow.
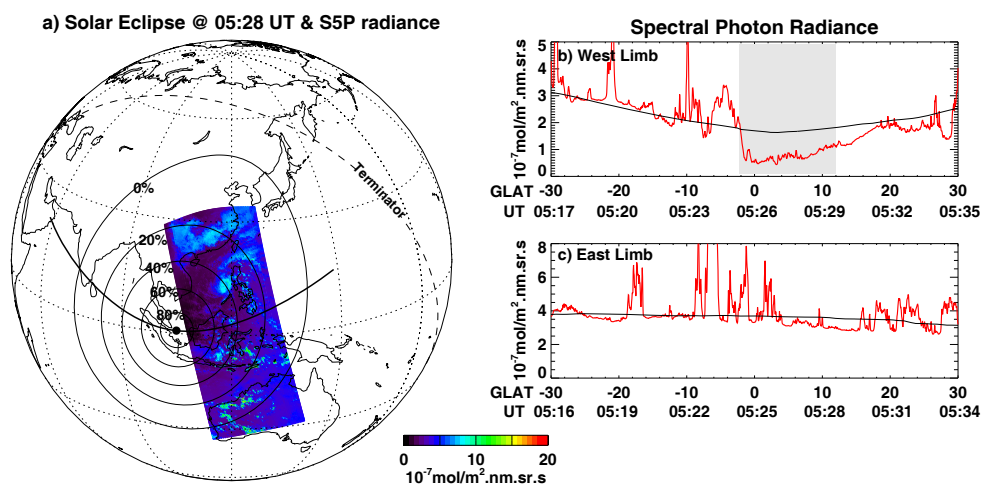
Figure 7. (a) A global map showing the annular solar eclipse path with a black dot representing the location of the greatest eclipse at 05:28 UT on 26 December 2019. Different obscuration lines and solar terminator are also shown. The spectral photon radiance in the UV-visible wavelength of 480 nm from S5P satellite between 05:15–05:35 UT is also plotted. (b and c) The latitudinal variation of the spectral radiance along the west and east limb of spectrometer scan, respectively. The shaded area represents significant radiance decrease relative to the background value due to the solar eclipse.

3.2 Space-borne Observations

To provide additional information beyond ground-based measurements, we also studied space-borne observations to further investigate the eclipse's moon shadow effect. In general, local ionospheric response to solar eclipse conditions is directly caused by reduced EUV heating and photo-ionization. Since there is no available measurement of eclipse-induced EUV variation at low-Earth orbit for the December 2019 event, we employed a proxy based procedure to estimate EUV input. Specifically, we first used UV lower atmosphere radiance data as measured by the S5P satellite to obtain a qualitative estimation of the EUV change in the ionosphere. Figure 7a shows spectral photon radiance in the UV-visible wavelength of 480 nm from the TROPOMI spectrometer on-board the S5P satellite during 05:15–05:35 UT on eclipse day. The annular eclipse location and associated obscuration lines at 05:28 UT are also marked. The cross-track swath of the spectrometer is 2600 km, which provides a good opportunity to see the eclipse-induced radiance reduction due to the obscuration difference between its west and east limbs. As can be seen from Figures 7a and 7b, the latitudinal variation of the radiance for the "near-eclipse" west limb exhibited a significant decrease ($\sim$60–80%) when S5P flew over the central eclipse region. On the other hand, the "far-from-eclipse" east limb only experienced weak obscuration ($<$20%) and thus exhibited a higher and more stable radiance level when compared with the west limb, after neglecting impulsive spikes due to cloud reflection.

–12–

Moreover, Figure 8a shows the solar obscuration distribution at 06:15 UT on eclipse day, as well as the corresponding satellite paths of DMSP F16 at ∼850 km and Swarm B at ∼500 km between 30°S–30°N. Both satellites were flying in ascending nodes at 15.8–16 LT, and were fortuitous to pass consecutively over the same shadow zone with only 3–5° longitudinal difference. The temporal consistency, horizontal collocation, and vertical separation of these orbital tracks allow us to investigate the altitude dependence of the eclipse-induced ionospheric response.

Figures 8b and 8d show the latitudinal variation of the in situ electron density (Ne) measurements during the eclipse day (Dec 26) and reference days for DMSP F16 and Swarm B, respectively. Figure 8c shows the associated electron temperature (Te) variation as measured by DMSP F16. Although both satellites intersected the 20%–40% shadow zone around 40 min before the local annular eclipse, they exhibit quite different variation patterns.

DMSP F16 at 850 km encountered an apparent Ne enhancement (∼30%) and Te decrease of 300–500 K relative to reference days. This cooling in electron temperature is an expected feature due to reduced EUV heating during the eclipse. Furthermore, Ne and Te in the topside ionosphere are typically negatively correlated with each other during the daytime in the low and mid latitude region if the external heating source is not large enough (e.g. Zhang & Holt, 2004; Bilitza et al., 2007; Su et al., 2015). Our results for the December eclipse are consistent with this inverse proportional relationship between Ne and Te.

In the near topside ionosphere, Swarm B at 500 km encountered a noticeable density reduction by ∼30–50% near the equatorial region. There was also a significant EIA widening phenomenon, and both northern and southern crest exhibited a clear poleward shift of 3–4°. Figure 7d shows the latitudinal variation of the up-looking TEC data derived from the GPS receiver on-board Swarm B. That data shows there was an average enhancement of 1–2 TECU during the eclipse day, in agreement with the Ne increase measured by DMSP at higher altitudes. In a collective sense, these results, including altitudinal discrepancy and EIA widening, demonstrate the presence of significant plasma gradients both horizontally and vertically in the topside ionosphere during the eclipse. This feature will be further discussed in the next section.

Finally, Figure 9 shows a second pass of DMSP and Swarm satellites over the equatorial region at ∼120°E around 07:45 UT, near the end time of local eclipse. Note that the local ionosphere has already gone through the eclipse even before satellite enter this region and catch up the fast-moving shadow. By comparing the shapes of different electron density profiles in Figure 9b and Figure 9d, it can be seen that the non-eclipse days did not exhibit clear EIA structure, while the eclipse day still maintained a pronounced double-crest structure at both DMSP and Swarm altitudes, which is consistent with the TEC enhancement at EIA crest shown in Figures 3–5. The DMSP still encountered a Ne enhancement and Te decrease relative to reference days.

4 Discussion

4.1 Equatorial local time eclipse response and counter-electrojet conditions

The December 2019 equatorial eclipse had several unique features. First, there was a larger TEC depletion and a longer recovery period in the equatorial morning sector than those of the midday sector during the eclipse. This unique equatorial local time effect is different from that typically seen in midlatitude eclipses. In particular, for a midlatitude eclipse, associated TEC/NmF2 depletions are typically larger around midday than in the morning, a feature usually attributed to higher background neutral concentrations and associated increases in ionospheric loss coefficients within the noon sector
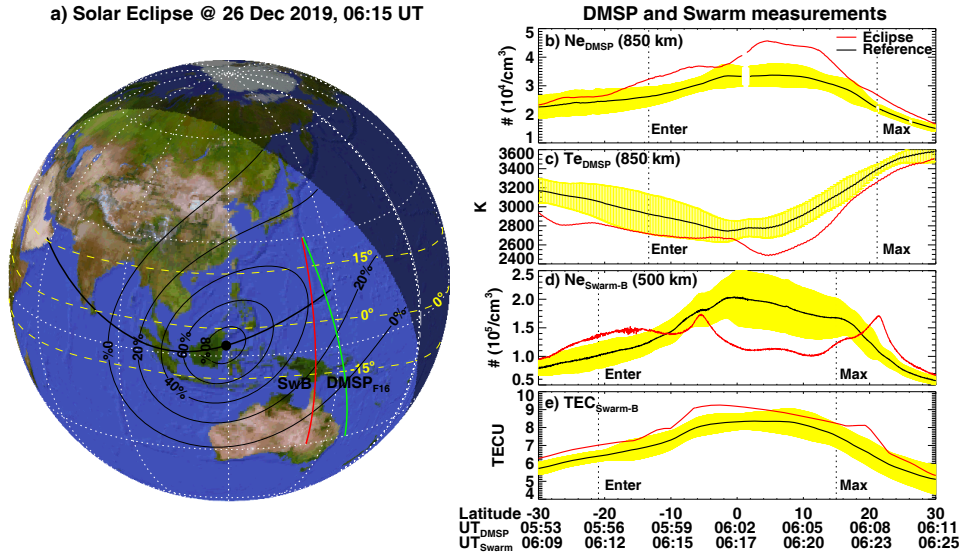
Figure 8. (a) A global map showing the annular solar eclipse path with a black dot representing the location of the greatest eclipse at 06:15 UT on 26 December 2019. Different obscuration zones (black line) as well as geomagnetic equator and $\pm 15°$ (yellow dashed lines) are also shown. The DMSP F16 path during 05:53–06:11 UT and Swarm B path during 06:09–06:25 are also plotted. (b–e) Latitudinal variation of the DMSP Ne, DMSP Te, Swarm Ne, and Swarm up-looking TEC during eclipse day (red) and reference days (black). The uncertainties of the reference values are marked with yellow error bars. Vertical lines mark the approximate location where the satellite enters the eclipse shadow, reaches maximum obscuration, and exits (if available).
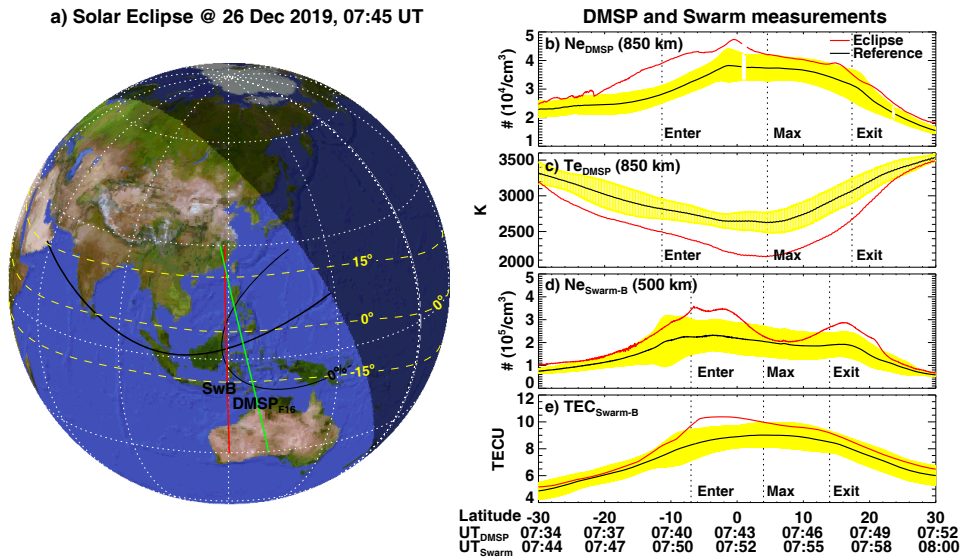
Figure 9. The same as Figure 8, but for eclipse interval at 07:45 UT, DMSP F16 path during 07:34–07:52 UT, and Swarm B path during 07:44–08:00 UT on 26 December 2019.

–14–

355 (Le et al., 2008b; Ding et al., 2010). However, eclipse impact in the equatorial ionosphere
356 is much more complicated compared to this scenario.

357   Several studies have indicated that an eclipse could induce rapid motion of low-pressure
358 systems and cause significant wind convergence, triggering a local neutral wind dynamo
359 that flows in a direction opposite to the normal daytime solar quiet (SQ) current sys-
360 tem, and this feature has been termed a counter-SQ current pattern (Choudhary et al.,
361 2011; St. -Maurice et al., 2011). Under these conditions, when the low-pressure system
362 center (maximum obscuration) approaches the magnetic equator, the equatorial electro-
363 jet (EEJ) will be largely weakened and sometimes even a full-blown counter electrojet
364 (CEJ) could be developed after the pass of maximum obscuration, a signature that fun-
365 damentally depends on competition between local and global dynamos (Cheng et al., 1992;
366 Tomás et al., 2007, 2008; Vyas & Sunda, 2012; Panda et al., 2015). In the December 2019
367 eclipse event under study, the annular eclipse center crossed the magnetic equator in the
368 early morning over Indian sector (see Figure 8a). The EEJ strength in the morning sec-
369 tor is usually very low, which provided a favorable condition for the counter-SQ current
370 system to generate CEJ through the processes mentioned above. The westward electric
371 field produced by the CEJ current pattern would cause a downward plasma drift, which
372 can intensify the eclipse-induced ionization decrease and effectively cut off the EIA sup-
373 ply. This scenario would generate a pronounced and prolonged local TEC depletion as
374 is shown in Figures 2–4.

375   Magnetometer based estimates of the equatorial electrojet further strengthen this
376 conclusion. A typical method to estimate local magnetic field variations and the strength
377 of equatorial electrojet is to subtract the horizontal magnetic field perturbations (ΔH)
378 measured by a low latitude magnetometer (i.e., Alibag) from those at another magne-
379 tometer near the magnetic equator (i.e., Tirunelveli) (Rastogi & Klobuchar, 1990). This
380 can remove global magnetic field fluctuations associated with ring currents. However,
381 the provisional data at the appropriate equatorial magnetometer of Tirunelveli is cur-
382 rently not available for the December 2019 eclipse due to long lag times in data updates.
383 Therefore, we employ another procedure given by Choudhary et al. (2011) and take ad-
384 vantage of the available and continuously calculated SYM-H index to remove global scale
385 magnetic contributions from two available magnetometer stations (Alibag and Kotota-
386 bang) as follows:

$$\Delta H = (H_{obs} - H_{2\sim3AM}) - C \times [SymH - SymH_{2\sim3AM}], \tag{1}$$

388 where the parameter C is the linear regression coefficient between the magnetometer lo-
389 cal perturbations and the SYM-H variations, derived using data for the entire month of
390 December during the local time period of 2–3 AM. For more details about this approach,
391 readers may refer to Choudhary et al. (2011) and St. -Maurice et al. (2011).

392   Figure 10a shows the derived ΔH variation at Alibag station during the eclipse day
393 (red line) and the monthly average (black line). In the first two hours on the eclipse day,
394 the ΔH fluctuated within the error envelope. However, with the start of the solar eclipse,
395 it showed an increasing diversion from the background trend and, after the maximum
396 eclipse, exhibited a statistically significant reduction in intensity. This continued for 6–
397 8 hours before recovery. These results imply that the daytime eastward current was weak-
398 ened substantially during and after eclipse passage, and provide compelling evidence for
399 eclipse-induced inhibition of equatorial electrojet in the Indian sector.

400   As a comparison, Figure 10b shows the ΔH variation at Kototabang station which
401 experienced a midday eclipse. Although the eclipse day curve fluctuated almost entirely
402 within the error envelope, a clear oscillation pattern was observed relative to the refer-
403 ence value. In particular, signatures seen include a considerable increase after eclipse start

–15–
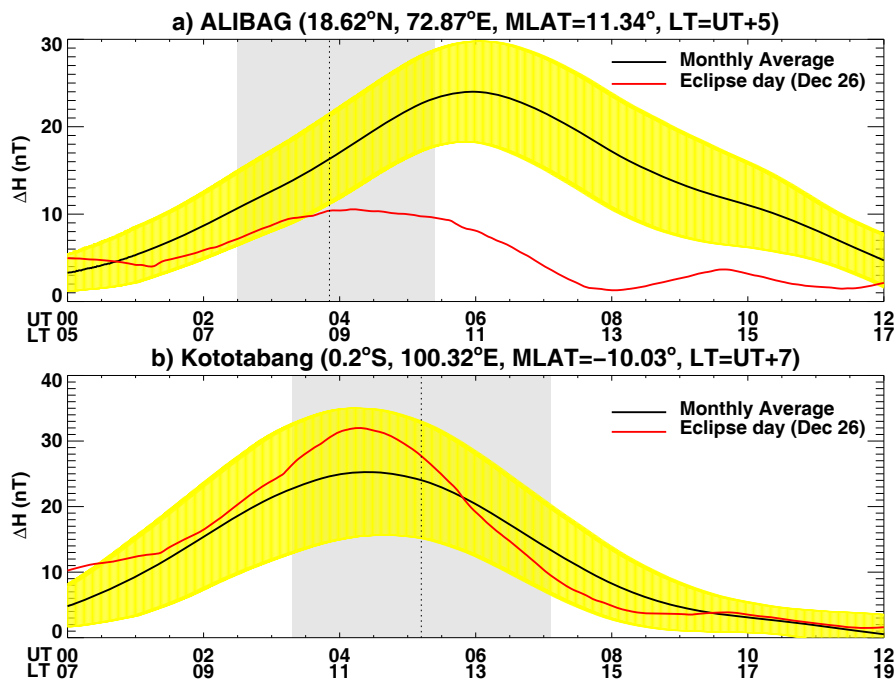
Figure 10. Diurnal variation of ΔH at (a) Alibag and (b) Kototabang stations for the eclipse day (red line) and the monthly average (black line). The one-σ deviations from the average are marked with yellow error bars. Data for the eclipse day (Dec 26) and magnetic disturbed days (Dec 18 and 19) were excluded from the statistics of monthly average. The shaded region shows the duration of the eclipse with the maximum time being marked by a vertical dotted line.

–16–

(corresponding to an enhanced eastward electric field), and a weaker reduction after eclipse maximum (corresponding to a westward electric field perturbation). This response will be further discussed in the next subsection.

We also note that both Alibag and Kototabang are not located in the magnetic equator, so the actual equatorial electrojet perturbations could be underestimated by this method. Nevertheless, by using Alibag and Kototabang data, our method provides strong qualitative evidence implying the presence of CEJ during the morning eclipse and the appearance of enhanced eastward electric field during the midday eclipse. Furthermore, this assertion is consistent with the observed "abnormal" local time effect previously discussed. In the future, further analysis can compute a quantitative specification of the electrojet perturbation magnitude, once real equatorial magnetometer data (i.e., Tirunelveli) for this event is available.

4.2 EIA crest enhancement and poleward shifting

We have identified a noticeable midday feature of EIA crest enhancement and poleward shifting in both hemispheres. This phenomenon could be collectively explained by one or more mechanistic reasons elucidated as follows.

(1) Eclipse-induced equatorward thermospheric winds: Thermospheric cooling and composition change due to decreased solar heating within the moon shadow area can generate thermospheric winds toward the eclipse region (Müller-Wodarg et al., 1998; Cnossen et al., 2019; Dang et al., 2018; Wang et al., 2019). For the studied equatorial eclipse event, the meridional wind component in the EIA crests is equatorward for both hemispheres, and this would raise plasma along the field lines to a higher altitude with fewer ion-neutral collisions and a correspondingly slower recombination rate (Anderson, 1976). This factor would enhance the local electron density. Such a mechanism has been verified by numerical simulations (Le et al., 2008b; Dang et al., 2020) and is consistent with observed EIA crest density increases, but we note that these equatorward disturbance wind effects would not easily explain EIA poleward shifting.

(2) Enhancement of the eastward electric field during the eclipse around the magnetic equator: Numerous previous studies have shown that near local sunset, the electric fields in the ionospheric E and F regions around the magnetic equator often show a strong eastward enhancement and upward plasma drift before the daytime field reverses to westward, due to the complex and time-dependent dynamics of conductivity variations near the terminator along magnetic field lines. This signature is well studied and is known as the prereversal enhancement (PRE) (Farley et al., 1986; Eccles, 1998; Eccles et al., 2015). In this sense, a solar eclipse is analogous to a very rapid local sunset, and its effect could trigger a quick decay of the conductivity in the lower E region due to the inhibition of ionization and the rapid recombination rate there (Rishbeth, 1968). Such a rapid change would cause the F region dynamo to respond and generate a strong downward polarization electric field. Combined with the curl-free requirement for the electric field, this would produce a corresponding zonal electric field as an edge effect and would drive an enhanced PRE-like vertical drift (Rishbeth, 1971a, 1971b; Eccles, 1998). Both our results in Figure 10b, along with previous observations and numerical simulations, have verified that solar eclipses can generate a considerable enhancement of the equatorial eastward electric field and upward plasma drift, especially in the heading (eastern) region of obscuration (Tsai & Liu, 1999; C.-H. Chen et al., 2019; L. P. Goncharenko et al., 2018; Dear et al., 2020). Under these conditions, the enhanced electric field and upward plasma drift would amplify the equatorial fountain effect and more rapidly evacuate the lower part of the F region (Tomás et al., 2007). This would increase the magnitude of EIA crest and also cause a poleward shift in its peak locations, similar to our direct observations.

–17–

For the current case, the F-region Ne profile measured by Swarm exhibited somewhat different behavior between two consecutive passes (comparing Figure 8d and Figure 9d) over the eclipse region. This might be due to the different dominant processes between electrodynamics and neutral winds. In particular, some studies reported that the maximum neutral wind/temperature responses lag behind totality for more than 30 min (e.g., Cnossen et al., 2019; Dang et al., 2018). For the first pass, the satellite flew over the eclipse leading (waxing) region (Figure 8a), and the neutral wind response lagged as mentioned above. Thus, the dominant eastward electric field perturbation and equatorial fountain effect caused a large Ne evacuation near the equator as well as considerable poleward shifting of EIA crests as shown in Figure 8d. For the second pass, the satellites flew over eclipse tailing (wading) region, the direction of electric field perturbation is expected to reverse, while the modified equatorward neutral wind pattern should reach its maximum and play a dominant role in raising plasma along field line to a higher altitude, thus leading to an overall larger Ne magnitude with enhanced EIA crests as shown in Figure 9d.

(3) Field-aligned plasma diffusion above the F2 peak: As mentioned previously, eclipse-induced ionosphere contraction at low latitudes will cause a reduction of plasma equilibrium scale height, leading to field-aligned plasma diffusion from the equatorial region to the EIA crest (Rishbeth, 1968; Ding et al., 2010). Additionally, previous studies have pointed out that the F2 layer around the EIA crest region is predominantly controlled by the fountain effect from the equator, rather than only by local solar eclipse effects (Cheng et al., 1992; Ding et al., 2010). This eclipse-induced field-aligned diffusion mechanism at low latitudes, combined with the enhanced upward fountain over the equator, would in aggregate enlarge the EIA crests through the processes mentioned above.

4.3 Altitude dependence of equatorial ionosphere eclipse response

Finally, the behavior of ionospheric Ne before the maximum eclipse exhibited a noticeable altitude difference over the equatorial region, with a considerable depletion around 500 km but an enhancement around 850 km with respect to reference days. This phenomenon could be explained by the following three reasons.

(1) The dip angle (latitude) effect of ionospheric response to solar eclipse (Le et al., 2009; G. Chen et al., 2011): The field-aligned diffusion process in general tends to compensate for eclipse-induced local depletion and to smooth out altitudinal difference at various layers, causing similar Ne reduction or enhancement at all heights in the F region and topside ionosphere (Rishbeth, 1968). However, this diffusion process has less downward component around the low and equatorial region than mid-latitudes, when considering the smaller magnetic inclination (dip angle) value near the equator (Le et al., 2008b; Ding et al., 2010). This factor implies that a transient eclipse-generated altitudinal gradient in the equatorial region cannot be effectively smoothed, especially during the darkening phase of the solar eclipse, and the resulting ionospheric state would likely to retain altitude-dependent electron density features.

(2) Enhanced eastward electric field and equatorward neutral wind during eclipse: As mentioned above, the enhanced eastward electric field over the equator can amplify the equatorial fountain effect, which evacuated F-region and pushed plasma upward to the topside ionosphere, generating plasma reduction near F2 peak and enhancements in the topside ionosphere (Lei et al., 2014, 2015). Moreover, the enhanced equatorward neutral wind also tends to push the low and mid- latitudes plasma near F2 region upward and equatorward, also contributing to the enhancement of the topside Ne and TEC around 800 km (C. H. Lin et al., 2005; Lei et al., 2016). On the other hand, the variation of integrated GNSS TEC in the eclipse region is more affected by the dominant response of F-layer and bottomside ionosphere, which showed a decrease mainly due to the reduced photo-ionization process.

–18–

Author Manuscript

(3) Negative correlation between Ne and Te at equatorial and low latitude ionosphere in the topside. The PRE-related vertical drift over the equatorial region and associated field-aligned diffusion toward EIA crest is strongly height dependent, which decays with altitude and becomes very weak at around 800–900 km (Pingree & Fejer, 1987; Eccles et al., 1999, 2015). Therefore, at DMSP altitude of 850 km, this inefficient vertical heat conduction helped in creating a quasi-steady state of thermal equilibrium, which is favorable in generating negatively correlated Te and Ne behavior as observed by many studies (e.g. Schunk & Nagy, 1978; Zhang & Holt, 2004; Zhang et al., 2004; Su et al., 2015). Therefore, during this equatorial eclipse event, a scenario at 850 km could emerge in which a initial Te decrease due to the inhibition of EUV heating, and a Ne enhancement created by wind and electric field, interact with each other and cause further Te reduction and Ne enhancement on the basis of above-mentioned anti-correlated mechanism. The quantitative strength of this feedback loop is unknown at the present, and more work in the future is needed to advance understanding on this potential altitude-dependent effect.

5 Conclusions

This paper studies the ionospheric response to an annular solar eclipse event on 26 December 2019 that traveled through equatorial latitudes in Asian longitude sectors. Using ground-based GNSS TEC and magnetometer data, as well as space-borne observations from Sentinel-5P, DMSP, and Swarm satellites, we have investigated ionospheric variations and associated electrodynamics with respect to obscuration, local time, latitude, and altitude at equatorial and EIA regions. The main results of this paper are summarized as follows:

1. There was a local UV spectral radiance reduction by ∼60–80% and a TEC depletion of ∼4–6 TECU (30–50%) along the annular eclipse path. Most depletion occurred within a 60% obscuration zone. The observed TEC decrease had a time lag after maximum eclipse obscuration ranging from several minutes to several dozens of minutes.

2. Contrary to a midlatitude eclipse scenario, this equatorial eclipse exhibited an "abnormal" local time effect along the eclipse path. Ionospheric TEC had a more pronounced depletion up to −6–8 TECU (∼50%) and longer recovery periods (∼4–6hr) in the morning than those in the midday, which are −4–6 TECU (30–40%) and ∼3 hour, respectively. The quantitative difference between photo-chemical and transport processes in the morning and midday sectors, as well as the ionospheric day-to-day variability including the unsettled geomagnetic condition at the beginning of the eclipse day, could possibly play a role. However, the eclipse-induced inhibition of the equatorial electrojet in the morning sector is likely to have made a considerable contribution.

3. A considerable EIA crest enhancement and poleward shifting occurred during the midday eclipse. Both northern and southern EIA crests exhibited 4–7 TECU (∼20–40%) enhancements and a 3–4° poleward shift. Besides normal influences from day-to-day variability, this phenomenon could be collectively generated by a combination of eclipse-induced equatorward thermospheric wind, enhanced eastward electric field, and enhanced field-aligned plasma diffusion above the F2 peak.

4. Before the arrival time of maximum eclipse obscuration, the equatorial ionospheric Ne exhibited a different vertical distribution pattern with ∼30% depletion around 500 km and ∼30% enhancement around 850 km. Electron temperature at 850 km showed a decrease of 300–500 K. Besides the latitudinal dependence of the field-aligned diffusion, this contrary Ne response is likely caused by the enhanced eastward electric field and equatorward neutral wind, combined with a fundamental anti-correlated relationship between Ne and Te in the topside ionosphere.

References

Aa, E., Huang, W., Liu, S., Shi, L., Gong, J., Chen, Y., & Shen, H. (2015). A regional ionospheric TEC mapping technique over China and adjacent areas: GNSS data processing and DINEOF analysis. *Sci. China Inf. Sci.*, *58*(10), 1-11. doi: 10.1007/s11432-015-5399-2

Aa, E., Huang, W., Yu, S., Liu, S., Shi, L., Gong, J., . . . Shen, H. (2015, June). A regional ionospheric TEC mapping technique over China and adjacent areas on the basis of data assimilation. *Journal of Geophysical Research (Space Physics)*, *120*(6), 5049-5061. doi: 10.1002/2015JA021140

Afraimovich, E. L., Palamartchouk, K. S., Perevalova, N. P., Chernukhov, V. V., Lukhnev, A. V., & Zalutsky, V. T. (1998, January). Ionospheric effects of

the solar eclipse of March 9, 1997, as deduced from GPS data. *Geophysical Research Letters*, *25*(4), 465-468. doi: 10.1029/98GL00186

Anderson, D. N. (1976, January). Modeling the midlatitude F-region ionospheric storm using east-west drift and a meridional wind. *Planet. Space Sci.*, *24*(1), 69-77. doi: 10.1016/0032-0633(76)90063-5

Basu, S., Basu, S., Huba, J., Krall, J., McDonald, S. E., Makela, J. J., ... Groves, K. (2009, April). Day-to-day variability of the equatorial ionization anomaly and scintillations at dusk observed by GUVI and modeling by SAMI3. *Journal of Geophysical Research: Space Physics*, *114*(A4), A04302. doi: 10.1029/2008JA013899

Bilitza, D., Truhlik, V., Richards, P., Abe, T., & Triskova, L. (2007, January). Solar cycle variations of mid-latitude electron density and temperature: Satellite measurements and model calculations. *Advances in Space Research*, *39*(5), 779-789. doi: 10.1016/j.asr.2006.11.022

Chen, C.-H., Lin, C.-H. C., & Matsuo, T. (2019, February). Ionospheric responses to the 21 August 2017 solar eclipse by using data assimilation approach. *Progress in Earth and Planetary Science*, *6*(1), 13. doi: 10.1186/s40645-019-0263-4

Chen, G., Qi, H., Ning, B., Zhao, Z., Yao, M., Deng, Z., ... Wu, C. (2013, October). Nighttime ionospheric enhancements induced by the occurrence of an evening solar eclipse. *Journal of Geophysical Research: Space Physics*, *118*(10), 6588-6596. doi: 10.1002/jgra.50551

Chen, G., Zhao, Z., Ning, B., Deng, Z., Yang, G., Zhou, C., ... Li, N. (2011, June). Latitudinal dependence of the ionospheric response to solar eclipse of 15 January 2010. *Journal of Geophysical Research*, *116*(A6), A06301. doi: 10.1029/2010JA016305

Cheng, K., Huang, Y.-N., & Chen, S.-W. (1992, January). Ionospheric effects of the solar eclipse of September 23, 1987, around the equatorial anomaly crest region. *Journal of Geophysical Research*, *97*(A1), 103-112. doi: 10.1029/91JA02409

Cherniak, I., & Zakharenkova, I. (2018, February). Ionospheric Total Electron Content Response to the Great American Solar Eclipse of 21 August 2017. *Geophysical Research Letters*, *45*(3), 1199-1208. doi: 10.1002/2017GL075989

Chimonas, G. (1970, January). Internal gravity-wave motions induced in the Earth's atmosphere by a solar eclipse. *Journal of Geophysical Research*, *75*(28), 5545. doi: 10.1029/JA075i028p05545

Choudhary, R. K., St. -Maurice, J. P., Ambili, K. M., Sunda, S., & Pathan, B. M. (2011, September). The impact of the January 15, 2010, annular solar eclipse on the equatorial and low latitude ionospheric densities. *Journal of Geophysical Research: Space Physics*, *116*(A9), A09309. doi: 10.1029/2011JA016504

Cnossen, I., Ridley, A. J., Goncharenko, L. P., & Harding, B. J. (2019, August). The Response of the Ionosphere-Thermosphere System to the 21 August 2017 Solar Eclipse. *Journal of Geophysical Research: Space Physics*, *124*(8), 7341-7355. doi: 10.1029/2018JA026402

Coster, A. J., Goncharenko, L., Zhang, S.-R., Erickson, P. J., Rideout, W., & Vierinen, J. (2017, December). GNSS Observations of Ionospheric Variations During the 21 August 2017 Solar Eclipse. *Geophysical Research Letters*, *44*(24), 12,041-12,048. doi: 10.1002/2017GL075774

Dang, T., Lei, J., Wang, W., Yan, M., Ren, D., & Huang, F. (2020). Prediction of the thermospheric and ionospheric responses to the 21 June 2020 annular solar eclipse. *Earth and Planetary Physics*, *4*(3), 1-7. doi: 10.26464/epp2020032

Dang, T., Lei, J., Wang, W., Zhang, B., Burns, A., Le, H., ... Wan, W. (2018, August). Global Responses of the Coupled Thermosphere and Ionosphere System to the August 2017 Great American Solar Eclipse. *Journal of Geophysical Research: Space Physics*, *123*(8), 7040-7050. doi: 10.1029/2018JA025566

Dear, V., Husin, A., Anggarani, S., Harjosuwito, J., & Pradipta, R. (2020). Iono-

spheric Effects During the Total Solar Eclipse Over Southeast Asia-Pacific on 9 March 2016: Part 1. Vertical Movement of Plasma Layer and Reduction in Electron Plasma Density. *Journal of Geophysical Research: Space Physics*, *125*(4), e2019JA026708. doi: 10.1029/2019JA026708

Ding, F., Wan, W., Ning, B., Liu, L., Le, H., Xu, G., ... Yang, M.   (2010, July). GPS TEC response to the 22 July 2009 total solar eclipse in East Asia. *Journal of Geophysical Research: Space Physics*, *115*(A7), A07308.   doi: 10.1029/2009JA015113

Eccles, J. V.   (1998, November).   A simple model of low-latitude electric fields. *Journal of Geophysical Research*, *103*(A11), 26699-26708.   doi: 10.1029/98JA02657

Eccles, J. V., Maynard, N., & Wilson, G.   (1999, January).   Study of the evening plasma drift vortex in the low-latitude ionosphere using San Marco electric field measurements. *Journal of Geophysical Research*, *104*(A12), 28133-28144. doi: 10.1029/1999JA900373

Eccles, J. V., St. Maurice, J. P., & Schunk, R. W.   (2015, June).   Mechanisms underlying the prereversal enhancement of the vertical plasma drift in the low-latitude ionosphere. *Journal of Geophysical Research: Space Physics*, *120*(6), 4950-4970. doi: 10.1002/2014JA020664

Eisenbeis, J., Occhipinti, G., Astafyeva, E., & Rolland , L. (2019, November). Short- and Long-Wavelength TIDs Generated by the Great American Eclipse of 21 August 2017. *Journal of Geophysical Research: Space Physics*, *124*(11), 9486-9493. doi: 10.1029/2019JA026919

Evans, J. V. (1965). On the behavior of fof2 during solar eclipses. *Journal of Geophysical Research*, *70*(3), 733-738. doi: 10.1029/JZ070i003p00733

Farley, D. T., Bonelli, E., Fejer, B. G., & Larsen, M. F.   (1986, December).   The prereversal enhancement of the zonal electric field in the equatorial ionosphere. *Journal of Geophysical Research*, *91*(A12), 13723-13728.   doi: 10.1029/JA091iA12p13723

Goncharenko, L., Harvey, V., Liu, H., & Pedatella, N.   (2020).   Sudden stratospheric warming impacts on the ionosphere-thermosphere system-a review of recent progress.   In *Space physics and aeronomy* (Vol. 3, chap. Advances in Ionospheric Research: Current Understanding and Challenges).   American Geophysical Union (AGU).

Goncharenko, L. P., Erickson, P. J., Zhang, S.-R., Galkin, I., Coster, A. J., & Jonah, O. F.   (2018, May).   Ionospheric Response to the Solar Eclipse of 21 August 2017 in Millstone Hill (42N) Observations. *Geophysical Research Letters*, *45*(10), 4601-4609. doi: 10.1029/2018GL077334

Harding, B. J., Drob, D. P., Buriti, R. A., & Makela, J. J.   (2018, April).   Nightside Detection of a Large-Scale Thermospheric Wave Generated by a Solar Eclipse. *Geophysical Research Letters*, *45*(8), 3366-3373. doi: 10.1002/2018GL077015

Hoque, M. M., Wenzel, D., Jakowski, N., Gerzen, T., Berdermann, J., Wilken, V., ... Minkwitz, D.   (2016, October).   Ionospheric response over Europe during the solar eclipse of March 20, 2015. *Journal of Space Weather and Space Climate*, *6*, A36. doi: 10.1051/swsc/2016032

Hu, L., Yue, X., & Ning, B. (2017, August). Development of the Beidou Ionospheric Observation Network in China for space weather monitoring. *Space Weather*, *15*(8), 974-984. doi: 10.1002/2017SW001636

Huang, C. R., Liu, C. H., Yeh, K. C., Lin, K. H., Tsai, W. H., Yeh, H. C., & Liu, J. Y.   (1999, January).   A study of tomographically reconstructed ionospheric images during a solar eclipse. *Journal of Geophysical Research*, *104*(A1), 79-94. doi: 10.1029/98JA02531

Huba, J. D., & Drob, D.   (2017, June).   SAMI3 prediction of the impact of the 21 August 2017 total solar eclipse on the ionosphere/plasmasphere system. *Geophysical Research Letters*, *44*(12), 5928-5935. doi: 10.1002/2017GL073549

–22–

Hussien, F., Ghamry, E., Fathy, A., & Mahrous, S. (2020, March). Swarm Satellite Observations of the 21 August 2017 Solar Eclipse. *Journal of Astronomy and Space Sciences*, *37*(1), 29-34. doi: 10.5140/JASS.2020.37.1.29

Jakowski, N., Stankov, S. M., Wilken, V., Borries, C., Altadill, D., Chum, J., . . . Cander, L. R. (2008, April). Ionospheric behavior over Europe during the solar eclipse of 3 October 2005. *Journal of Atmospheric and Solar-Terrestrial Physics*, *70*(6), 836-853. doi: 10.1016/j.jastp.2007.02.016

Jonah, O. F., Goncharenko, L., Erickson, P. J., Zhang, S., Coster, A., Chau, J. L., . . . Rideout, W. (2020). Anomalous behavior of the equatorial ionization anomaly during the july 2, 2019 solar eclipse. *Journal of Geophysical Research: Space Physics*, *125*, e2020JA027909. doi: 10.1029/2020JA027909

Kikuchi, T., Hashimoto, K. K., & Nozaki, K. (2008, June). Penetration of magnetospheric electric fields to the equator during a geomagnetic storm. *Journal of Geophysical Research: Space Physics*, *113*(A6), A06214. doi: 10.1029/2007JA012628

Le, H., Liu, L., Yue, X., & Wan, W. (2008a, February). The ionospheric responses to the 11 August 1999 solar eclipse: observations and modeling. *Annales Geophysicae*, *26*(1), 107-116. doi: 10.5194/angeo-26-107-2008

Le, H., Liu, L., Yue, X., & Wan, W. (2008b, August). The midlatitude F2 layer during solar eclipses: Observations and modeling. *Journal of Geophysical Research*, *113*(A8), A08309. doi: 10.1029/2007JA013012

Le, H., Liu, L., Yue, X., Wan, W., & Ning, B. (2009, July). Latitudinal dependence of the ionospheric response to solar eclipses. *Journal of Geophysical Research*, *114*(A7), A07308. doi: 10.1029/2009JA014072

Lei, J., Dang, T., Wang, W., Burns, A., Zhang, B., & Le, H. (2018, May). Long-Lasting Response of the Global Thermosphere and Ionosphere to the 21 August 2017 Solar Eclipse. *Journal of Geophysical Research: Space Physics*, *123*(5), 4309-4316. doi: 10.1029/2018JA025460

Lei, J., Huang, F., Chen, X., Zhong, J., Ren, D., Wang, W., . . . Xue, X. (2018, April). Was Magnetic Storm the Only Driver of the Long-Duration Enhancements of Daytime Total Electron Content in the Asian-Australian Sector Between 7 and 12 September 2017? *Journal of Geophysical Research: Space Physics*, *123*(4), 3217-3232. doi: 10.1029/2017JA025166

Lei, J., Wang, W., Burns, A. G., Yue, X., Dou, X., Luan, X., . . . Liu, Y. C. M. (2014, March). New aspects of the ionospheric response to the October 2003 superstorms from multiple-satellite observations. *Journal of Geophysical Research: Space Physics)*, *119*(3), 2298-2317. doi: 10.1002/2013JA019575

Lei, J., Zhong, J., Mao, T., Hu, L., Yu, T., Luan, X., . . . Batista, I. S. (2016, October). Contrasting behavior of the F_2 peak and the topside ionosphere in response to the 2 October 2013 geomagnetic storm. *Journal of Geophysical Research: Space Physics*, *121*(10), 10,549-10,563. doi: 10.1002/2016JA022959

Lei, J., Zhu, Q., Wang, W., Burns, A. G., Zhao, B., Luan, X., . . . Dou, X. (2015, August). Response of the topside and bottomside ionosphere at low and middle latitudes to the October 2003 superstorms. *Journal of Geophysical Research: Space Physics*, *120*(8), 6974-6986. doi: 10.1002/2015JA021310

Lin, C. H., Richmond, A. D., Heelis, R. A., Bailey, G. J., Lu, G., Liu, J. Y., . . . Su, S. Y. (2005, December). Theoretical study of the low- and midlatitude ionospheric electron density enhancement during the October 2003 superstorm: Relative importance of the neutral wind and the electric field. *Journal of Geophysical Research: Space Physics*, *110*(A12), A12312. doi: 10.1029/2005JA011304

Lin, C. Y., Deng, Y., & Ridley, A. (2018, June). Atmospheric Gravity Waves in the Ionosphere and Thermosphere During the 2017 Solar Eclipse. *Geophysical Research Letters*, *45*(11), 5246-5252. doi: 10.1029/2018GL077388

Liu, J., Hsiao, C., Tsai, L., Liu, C., Kuo, F., Lue, H., & Huang, C. (1998). Vertical

–23–

phase and group velocities of internalgravity waves derived from ionograms during the solareclipse of 24 october 1995. *Journal of Atmospheric and Solar-Terrestrial Physics*, *60*(17), 1679 - 1686. doi: 10.1016/S1364-6826(98)00103-5

Liu, J. Y., Sun, Y. Y., Kakinami, Y., Chen, C. H., Lin, C. H., & Tsai, H. F. (2011, September). Bow and stern waves triggered by the Moon's shadow boat. *Geophysical Research Letters*, *38*(17), L17109. doi: 10.1029/2011GL048805

Liu, L., Zou, S., Yao, Y., & Aa, E. (2020). Multi-scale ionosphere responses to the May 2017 magnetic storm over the Asian sector. *GPS Solutions*, *24*, 26. doi: 10.1007/s10291-019-0940-1

MacPherson, B., González, S. A., Sulzer, M. P., Bailey, G. J., Djuth, F., & Rodriguez, P. (2000). Measurements of the topside ionosphere over Arecibo during the total solar eclipse of February 26, 1998. *Journal of Geophysical Research*, *105*(A10), 23055-23068. doi: 10.1029/2000JA000145

Momani, M. A., Yatim, B., & Mohd Ali, M. A. (2010, August). Ionospheric and geomagnetic response to the total solar eclipse on 1 August 2008 over Northern Hemisphere. *Journal of Geophysical Research*, *115*(A8), A08321. doi: 10.1029/2009JA014999

Mrak, S., Semeter, J., Nishimura, Y., Hirsch, M., & Sivadas, N. (2018, October). Coincidental TID Production by Tropospheric Weather During the August 2017 Total Solar Eclipse. *Geophysical Research Letters*, *45*(20), 10,903-10,911. doi: 10.1029/2018GL080239

Müller-Wodarg, I. C. F., Aylward, A. D., & Lockwood, M. (1998, January). Effects of a mid-latitude solar eclipse on the thermosphere and ionosphere - A modelling study. *Geophysical Research Letters*, *25*(20), 3787-3790. doi: 10.1029/1998GL900045

Nayak, C., & Yiğit, E. (2018, January). GPS-TEC Observation of Gravity Waves Generated in the Ionosphere During 21 August 2017 Total Solar Eclipse. *Journal of Geophysical Research: Space Physics*, *123*(1), 725-738. doi: 10.1002/2017JA024845

Panda, S. K., Gedam, S. S., Rajaram, G., Sripathi, S., & Bhaskar, A. (2015, December). Impact of the 15 January 2010 annular solar eclipse on the equatorial and low latitude ionosphere over the Indian region. *Journal of Atmospheric and Solar-Terrestrial Physics*, *135*, 181-191. doi: 10.1016/j.jastp.2015.11.004

Perry, G. W., Watson, C., Howarth, A. D., Themens, D. R., Foss, V., Langley, R. B., & Yau, A. W. (2019, July). Topside Ionospheric Disturbances Detected Using Radio Occultation Measurements During the August 2017 Solar Eclipse. *Geophysical Research Letters*, *46*(13), 7069-7078. doi: 10.1029/2019GL083195

Pingree, J. E., & Fejer, B. G. (1987, May). On the height variation of the equatorial F region vertical plasma drifts. *Journal of Geophysical Research*, *92*(A5), 4763-4766. doi: 10.1029/JA092iA05p04763

Pradipta, R., Yizengaw, E., & Doherty, P. (2018, August). Ionospheric Density Irregularities, Turbulence, and Wave Disturbances During the Total Solar Eclipse Over North America on 21 August 2017. *Geophysical Research Letters*, *45*(16), 7909-7917. doi: 10.1029/2018GL079383

Rastogi, R. G., & Klobuchar, J. A. (1990, November). Ionospheric electron content within the equatorial F_2 layer anomaly belt. *Journal of Geophysical Research*, *95*(A11), 19045-19052. doi: 10.1029/JA095iA11p19045

Reinisch, B. W., Dandenault, P. B., Galkin, I. A., Hamel, R., & Richards, P. G. (2018, February). Investigation of the Electron Density Variation During the 21 August 2017 Solar Eclipse. *Geophysical Research Letters*, *45*(3), 1253-1261. doi: 10.1002/2017GL076572

Rideout, W., & Coster, A. (2006). Automated gps processing for global total electron content data. *GPS Solut.*, *10*(3), 219-228. doi: 10.1007/s10291-006-0029-5

Rishbeth, H. (1968, September). Solar Eclipses and Ionospheric Theory. *Space Sci.*

–24–

827   *Rev.*, *8*(4), 543-554. doi: 10.1007/BF00175006

828   Rishbeth, H. (1971a, February). The F-layer dynamo. *Planet. Space Sci.*, *19*(2), 263-
829   267. doi: 10.1016/0032-0633(71)90205-4

830   Rishbeth, H. (1971b, March). Polarization fields produced by winds in the equatorial
831   F-region. *Planet. Space Sci.*, *19*(3), 357-369. doi: 10.1016/0032-0633(71)90098
832   -5

833   Rishbeth, H., Jenkins, B., & Moffett, R. J. (1995). The F-layer at sunrise. *Annales
834   Geophysicae*, *13*(4), 367–374.

835   Salah, J. E., Oliver, W. L., Foster, J. C., Holt, J. M., Emery, B. A., & Roble,
836   R. G. (1986). Observations of the May 30, 1984, annular solar eclipse at
837   Millstone Hill. *Journal of Geophysical Research*, *91*(A2), 1651-1660. doi:
838   10.1029/JA091iA02p01651

839   Schunk, R. W., & Nagy, A. F. (1978, August). Electron temperatures in the F
840   region of the ionosphere: theory and observation. *Reviews of Geophysics and
841   Space Physics*, *16*, 355-399. doi: 10.1029/RG016i003p00355

842   St. -Maurice, J. P., Ambili, K. M., & Choudhary, R. K. (2011, February). Lo-
843   cal electrodynamics of a solar eclipse at the magnetic equator in the early
844   afternoon hours. *Geophysical Research Letters*, *38*(4), L04102. doi:
845   10.1029/2010GL046085

846   Su, F., Wang, W., Burns, A. G., Yue, X., & Zhu, F. (2015, December). The cor-
847   relation between electron temperature and density in the topside ionosphere
848   during 2006-2009. *Journal of Geophysical Research: Space Physics*, *120*(12),
849   10,724-10,739. doi: 10.1002/2015JA021303

850   Sun, Y.-Y., Liu, J.-Y., Lin, C. C.-H., Lin, C.-Y., Shen, M.-H., Chen, C.-H., . . .
851   Chou, M.-Y. (2018, January). Ionospheric Bow Wave Induced by the Moon
852   Shadow Ship Over the Continent of United States on 21 August 2017. *Geo-
853   physical Research Letters*, *45*(2), 538-544. doi: 10.1002/2017GL075926

854   Tomás, A. T., Lühr, H., FöRster, M., Rentz, S., & Rother, M. (2007, June). Ob-
855   servations of the low-latitude solar eclipse on 8 April 2005 by CHAMP. *Jour-
856   nal of Geophysical Research*, *112*(A6), A06303. doi: 10.1029/2006JA012168

857   Tomás, A. T., Lühr, H., Rother, M., Manoj, C., Olsen, N., & Watari, S. (2008, Au-
858   gust). What are the influences of solar eclipses on the equatorial electrojet?
859   *Journal of Atmospheric and Solar-Terrestrial Physics*, *70*(11-12), 1497-1511.
860   doi: 10.1016/j.jastp.2008.05.009

861   Tsai, H. F., & Liu, J. Y. (1999, June). Ionospheric total electron content response to
862   solar eclipses. *Journal of Geophysical Research*, *104*(A6), 12657-12668. doi: 10
863   .1029/1999JA900001

864   Veefkind, J. P., Aben, I., McMullan, K., Förster, H., de Vries, J., Otter, G., . . . Lev-
865   elt, P. F. (2012, May). TROPOMI on the ESA Sentinel-5 Precursor: A GMES
866   mission for global observations of the atmospheric composition for climate, air
867   quality and ozone layer applications. *Remote Sensing of Environment*, *120*,
868   70-83. doi: 10.1016/j.rse.2011.09.027

869   Vierinen, J., Coster, A. J., Rideout, W. C., Erickson, P. J., & Norberg, J. (2016).
870   Statistical framework for estimating GNSS bias. *Atmospheric Measurement
871   Techniques*, *9*, 1303-1312. doi: 10.5194/amt-9-1303-2016

872   Vyas, B. M., & Sunda, S. (2012, February). The solar eclipse and its associated
873   ionospheric TEC variations over Indian stations on January 15, 2010. *Advances
874   in Space Research*, *49*(3), 546-555. doi: 10.1016/j.asr.2011.11.009

875   Wang, W., Dang, T., Lei, J., Zhang, S., Zhang, B., & Burns, A. (2019, April). Phys-
876   ical Processes Driving the Response of the F_2 Region Ionosphere to the 21
877   August 2017 Solar Eclipse at Millstone Hill. *Journal of Geophysical Research:
878   Space Physics*, *124*(4), 2978-2991. doi: 10.1029/2018JA025479

879   Wu, C., Ridley, A. J., Goncharenko, L., & Chen, G. (2018, April). GITM-
880   Data Comparisons of the Depletion and Enhancement During the 2017
881   Solar Eclipse. *Geophysical Research Letters*, *45*(8), 3319-3327. doi:

–25–

10.1002/2018GL077409

Yau, A. W., Foss, V., Howarth, A. D., Perry, G. W., Watson, C., & Huba, J. (2018, October). Eclipse-Induced Changes to Topside Ion Composition and Field-Aligned Ion Flows in the August 2017 Solar Eclipse: e-POP Observations. *Geophysical Research Letters*, *45*(20), 10,829-10,837. doi: 10.1029/2018GL079269

Zhang, S.-R., Erickson, P. J., Goncharenko, L. P., Coster, A. J., Rideout, W., & Vierinen, J. (2017, December). Ionospheric Bow Waves and Perturbations Induced by the 21 August 2017 Solar Eclipse. *Geophysical Research Letters*, *44*(24), 12,067-12,073. doi: 10.1002/2017GL076054

Zhang, S.-R., & Holt, J. M. (2004, January). Ionospheric plasma temperatures during 1976-2001 over Millstone Hill. *Advances in Space Research*, *33*(6), 963-969. doi: 10.1016/j.asr.2003.07.012

Zhang, S.-R., Holt, J. M., Zalucha, A. M., & Amory-Mazaudier, C. (2004, November). Midlatitude ionospheric plasma temperature climatology and empirical model based on Saint Santin incoherent scatter radar data from 1966 to 1987. *Journal of Geophysical Research: Space Physics*, *109*(A11), A11311. doi: 10.1029/2004JA010709

Figure 1.

a) F10.7

b) Kp

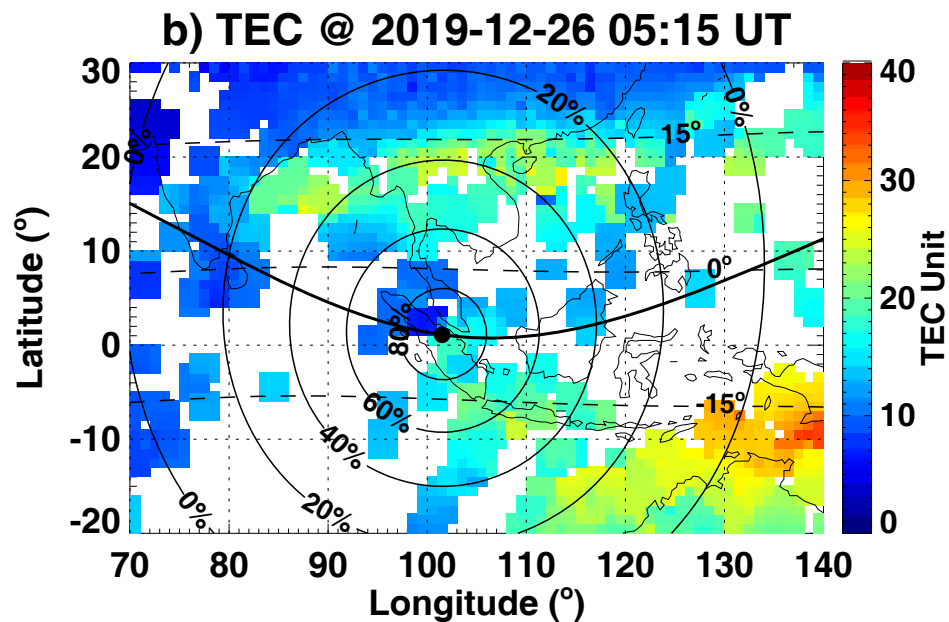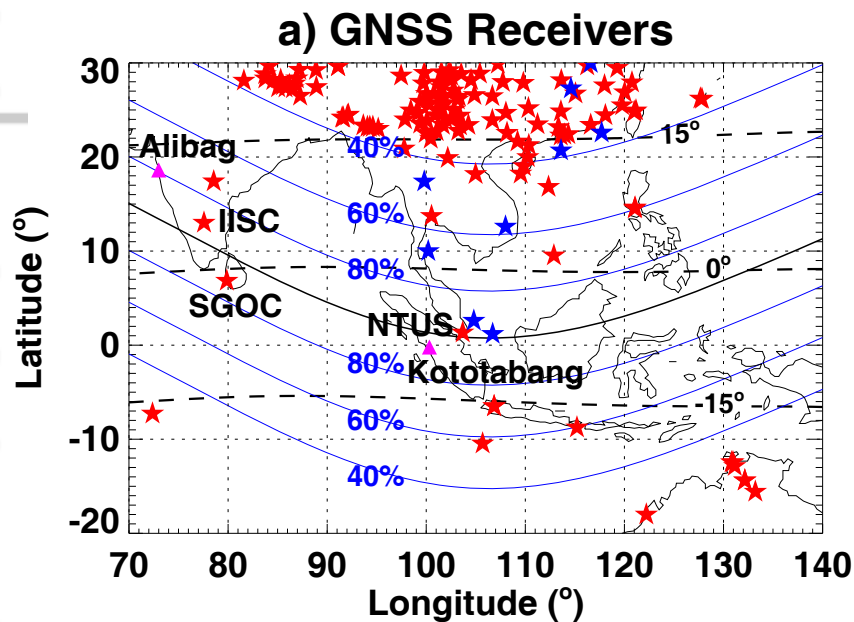c) IMF Bz

d) IEF

e) Dst

December 2019

Figure 2.

a) GNSS Receivers
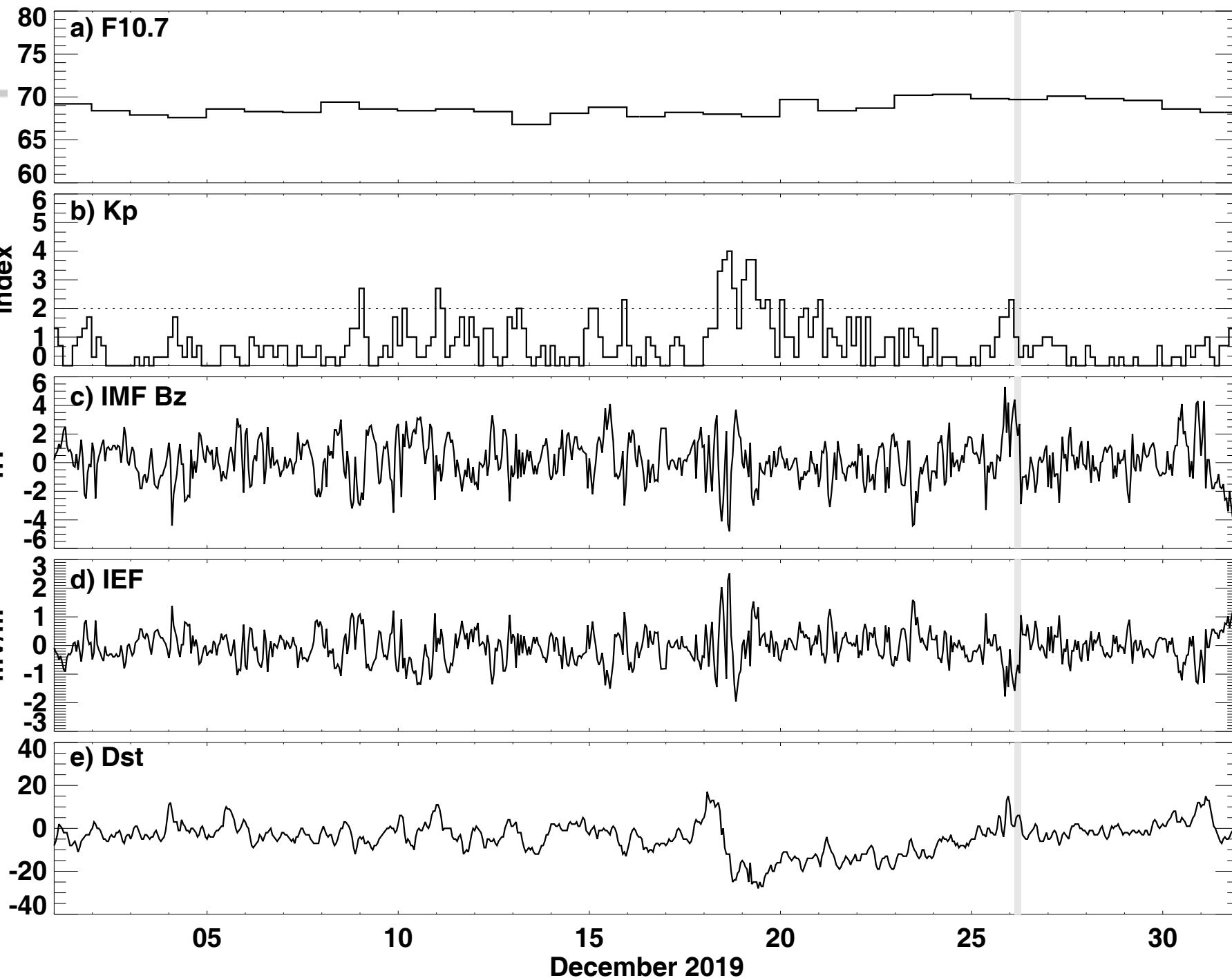
b) TEC @ 2019-12-26 05:15 UT

IISC (12.9°N, 77.6°E, 6.5°MLAT)

SGOC (6.9°N, 79.9°E, -1.5°MLAT)

NTUS (1.3°N, 103.7°E, -6.9°MLAT)
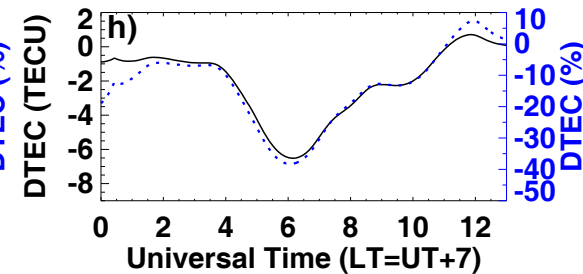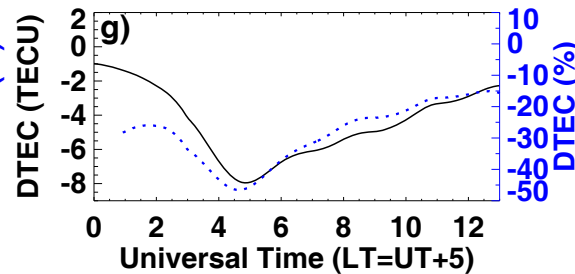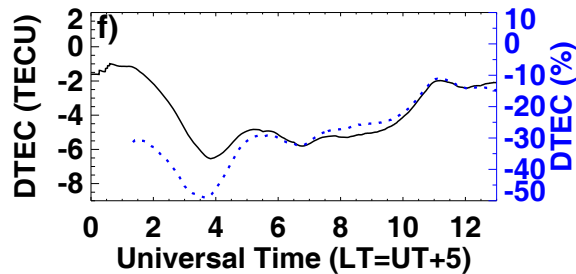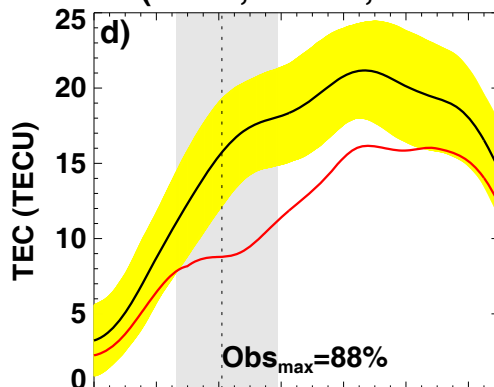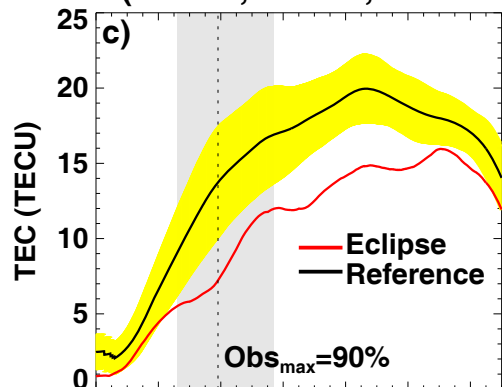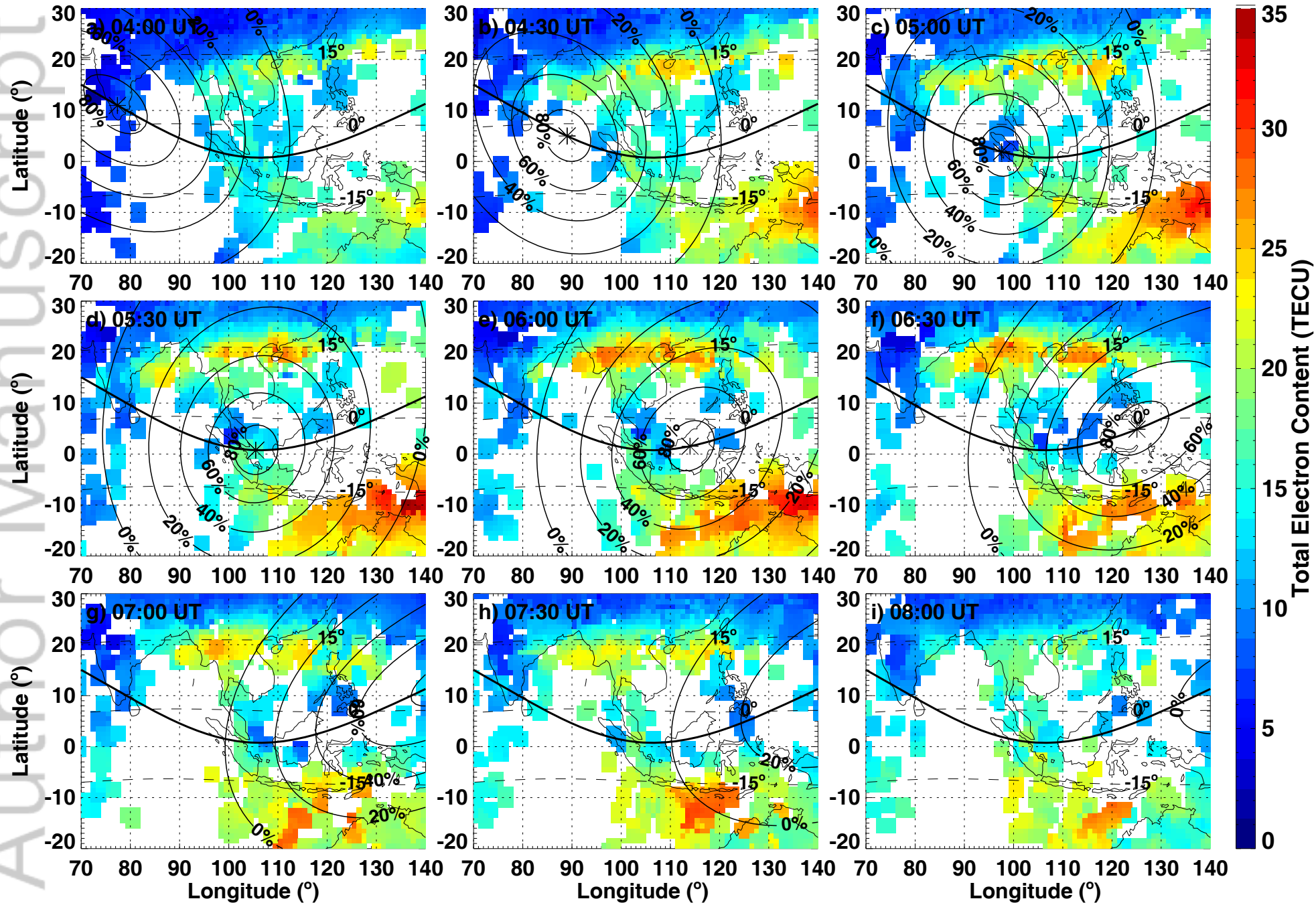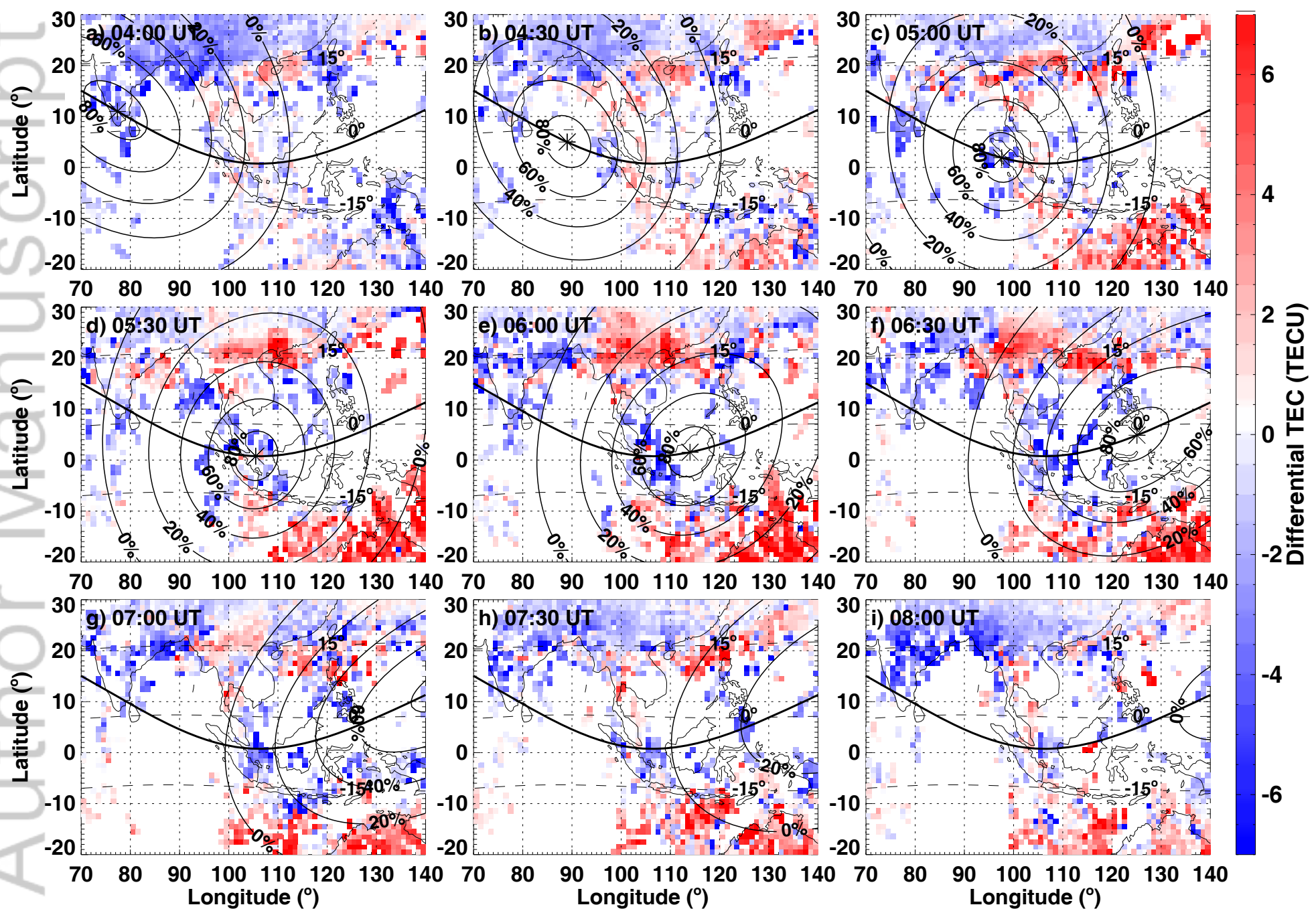
c) Obs$_{max}$=90%

d) Obs$_{max}$=88%
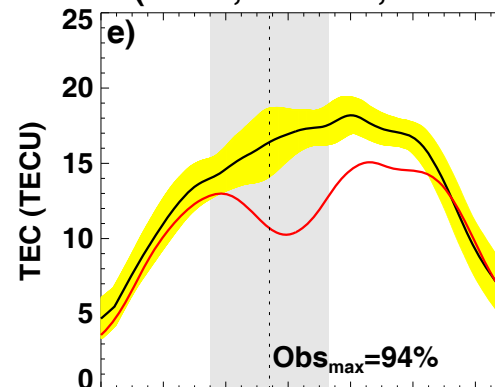
e) Obs$_{max}$=94%

Eclipse
Reference

Figure 3.

Figure 4.

Figure 5.

Differential TEC

a) 095°E

b) 105°E

c) 115°E

Absolute TEC

d) 095°E

e) 105°E

f) 115°E

Reference TEC

g) 095°E

h) 105°E

i) 115°E

Figure 6.

(a) BBKD (30.3N,116.6E, MLAT 23.7N), LT = UT+7.8

(b) HSKD (27.3N,114.6E, MLAT 20.6N), LT = UT+7.6

(c) KMNM (22.6N,117.7E, MLAT 15.6N), LT = UT+7.8

(d) HKSL (20.7N,113.6E, MLAT 13.7N), LT = UT+7.6

(e) CMUM (17.4N,99.8E, MLAT 9.9N), LT = UT+6.7

(f) CUSV (12.6N,108.0E, MLAT 4.9N), LT = UT+7.2

(g) CPNM (10.0N,100.2E, MLAT 1.8N), LT = UT+6.7

(h) ANMG (2.6N,104.8E, MLAT 6.1S), LT = UT+7.0

(i) SIN1 (1.2N,106.7E, MLAT 7.5S), LT = UT+7.1

GEO TEC (TECU)

December 2019
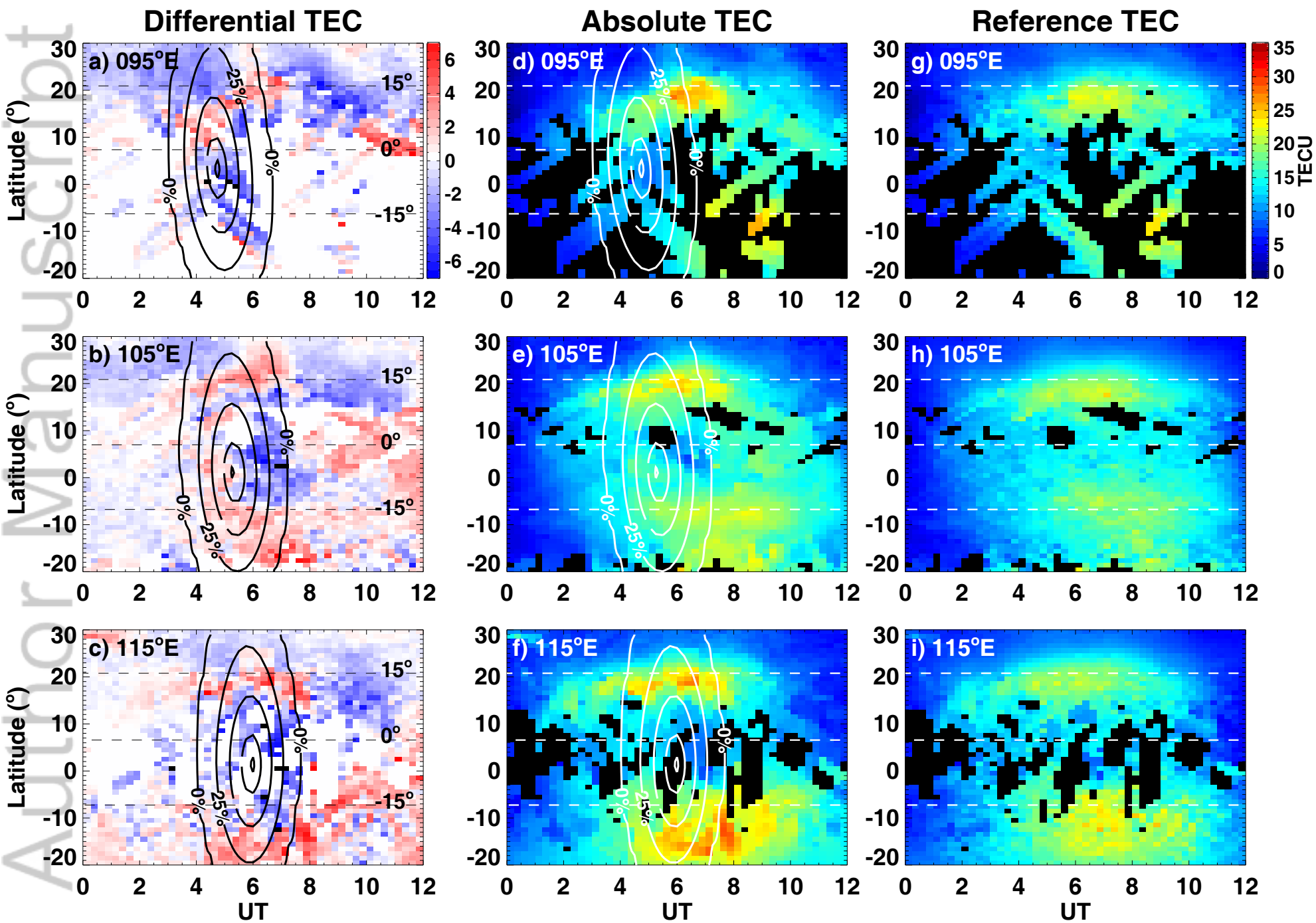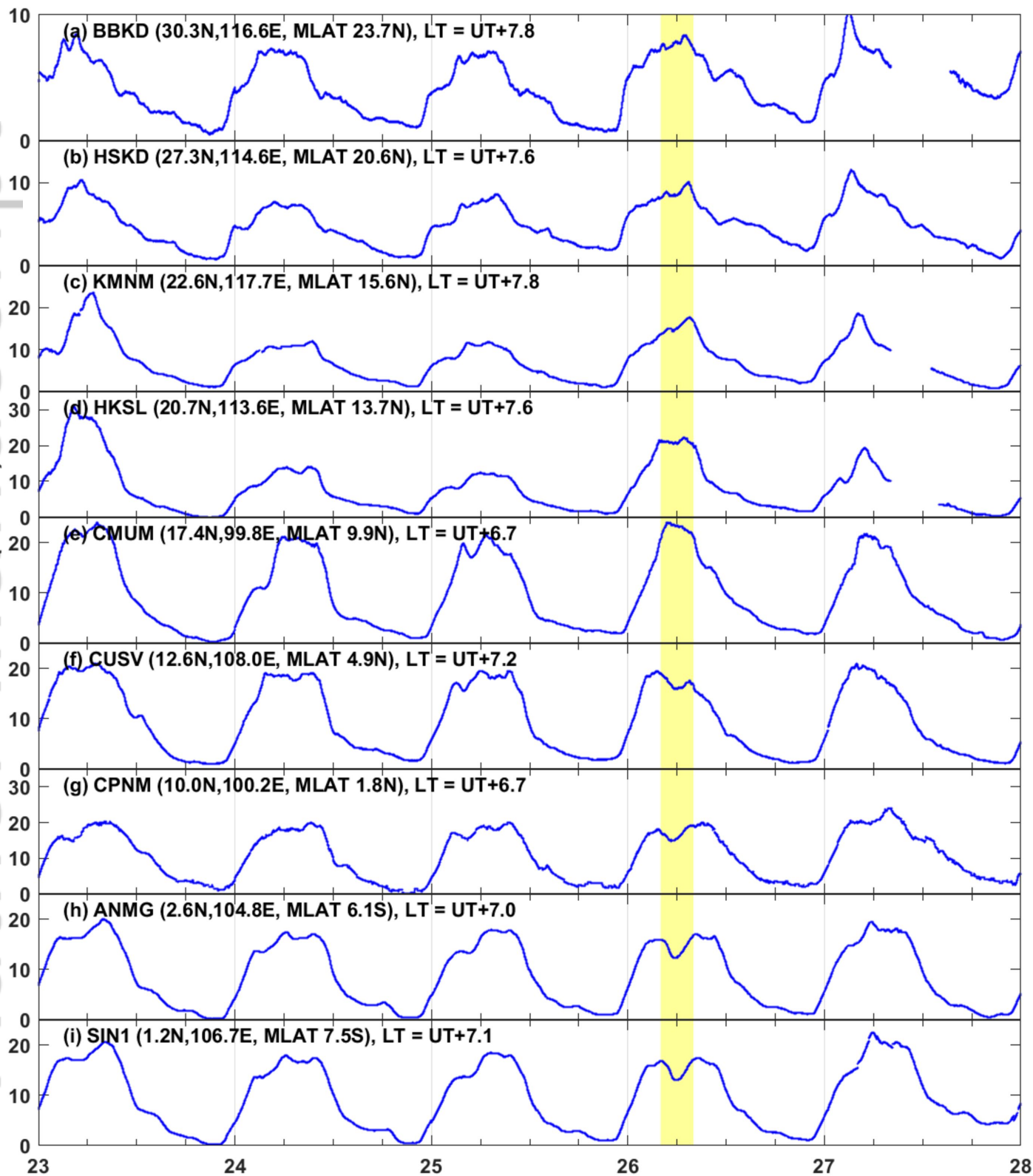
Figure 7.

a) Solar Eclipse @ 05:28 UT & S5P radiance
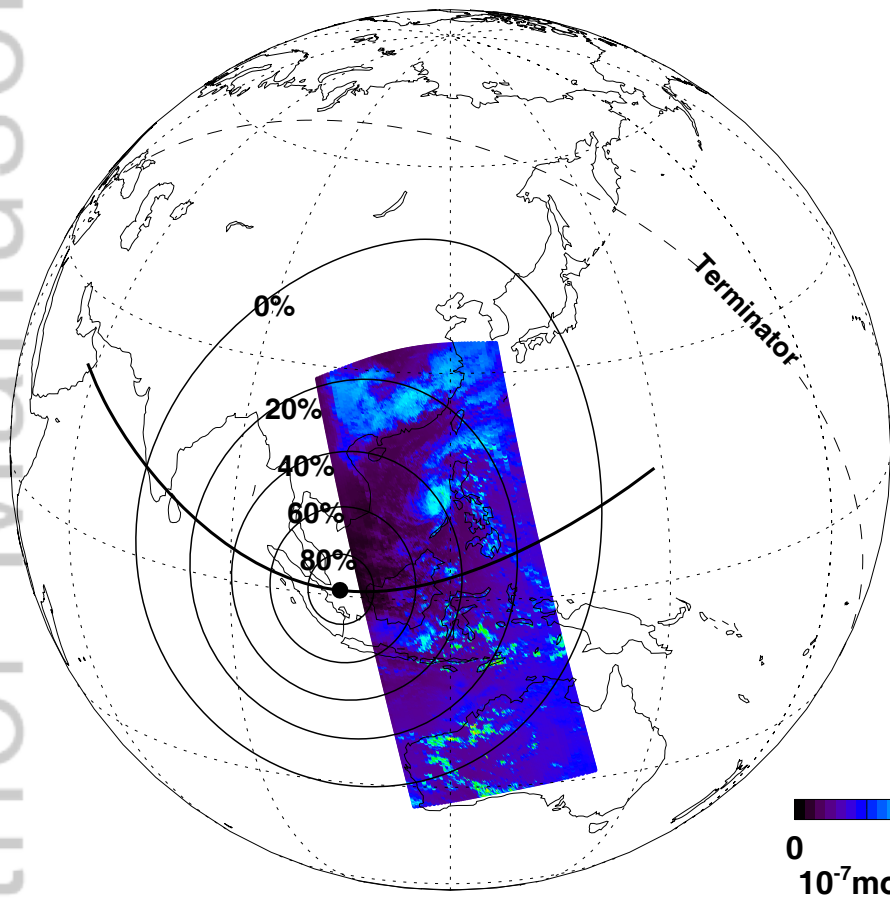
Spectral Photon Radiance
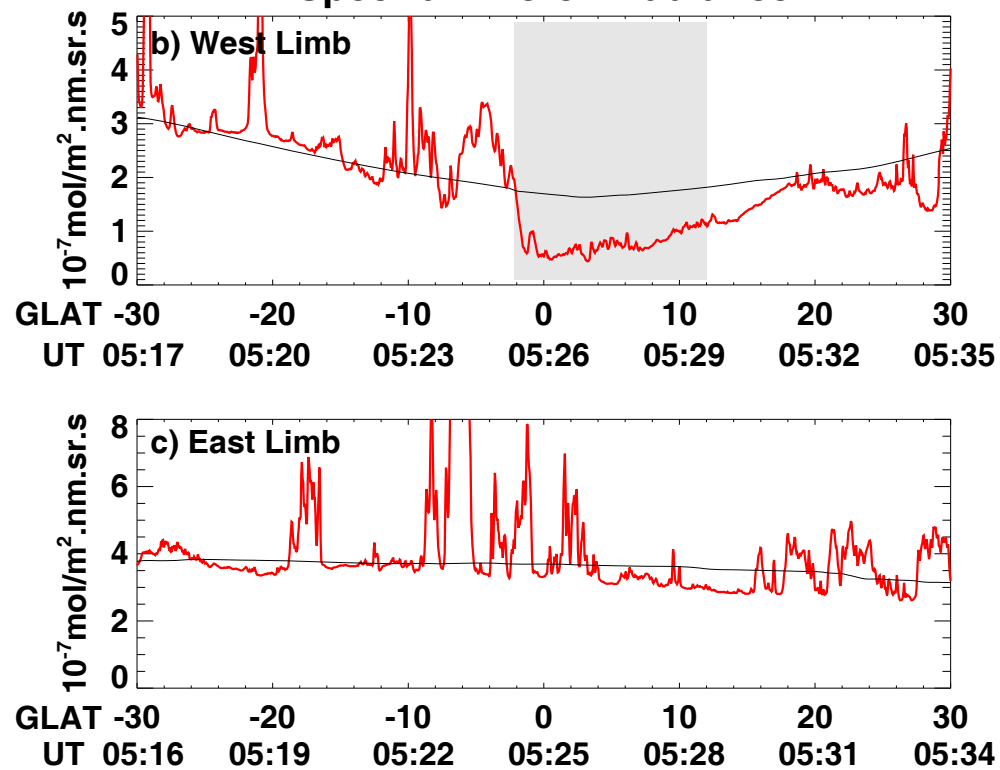
b) West Limb

c) East Limb

Figure 8.

a) Solar Eclipse @ 26 Dec 2019, 06:15 UT

DMSP and Swarm measurements

b) Ne_{DMSP} (850 km)
c) Te_{DMSP} (850 km)
d) $Ne_{Swarm-B}$ (500 km)
e) $TEC_{Swarm-B}$

Eclipse
Reference

Enter
Max

SwB
$DMSP_{F16}$

Latitude	-30	-20	-10	0	10	20	30
UT_{DMSP}	05:53	05:56	05:59	06:02	06:05	06:08	06:11
UT_{Swarm}	06:09	06:12	06:15	06:17	06:20	06:23	06:25

Figure 9.

a) Solar Eclipse @ 26 Dec 2019, 07:45 UT

DMSP and Swarm measurements

b) Ne$_{DMSP}$ (850 km)

— Eclipse
— Reference

(10^4/cm^3)

Enter   Max   Exit

c) Te$_{DMSP}$ (850 km)

K

Enter   Max   Exit

d) Ne$_{Swarm-B}$ (500 km)

(10^5/cm^3)

Enter   Max   Exit

e) TEC$_{Swarm-B}$

TECU

Enter   Max   Exit

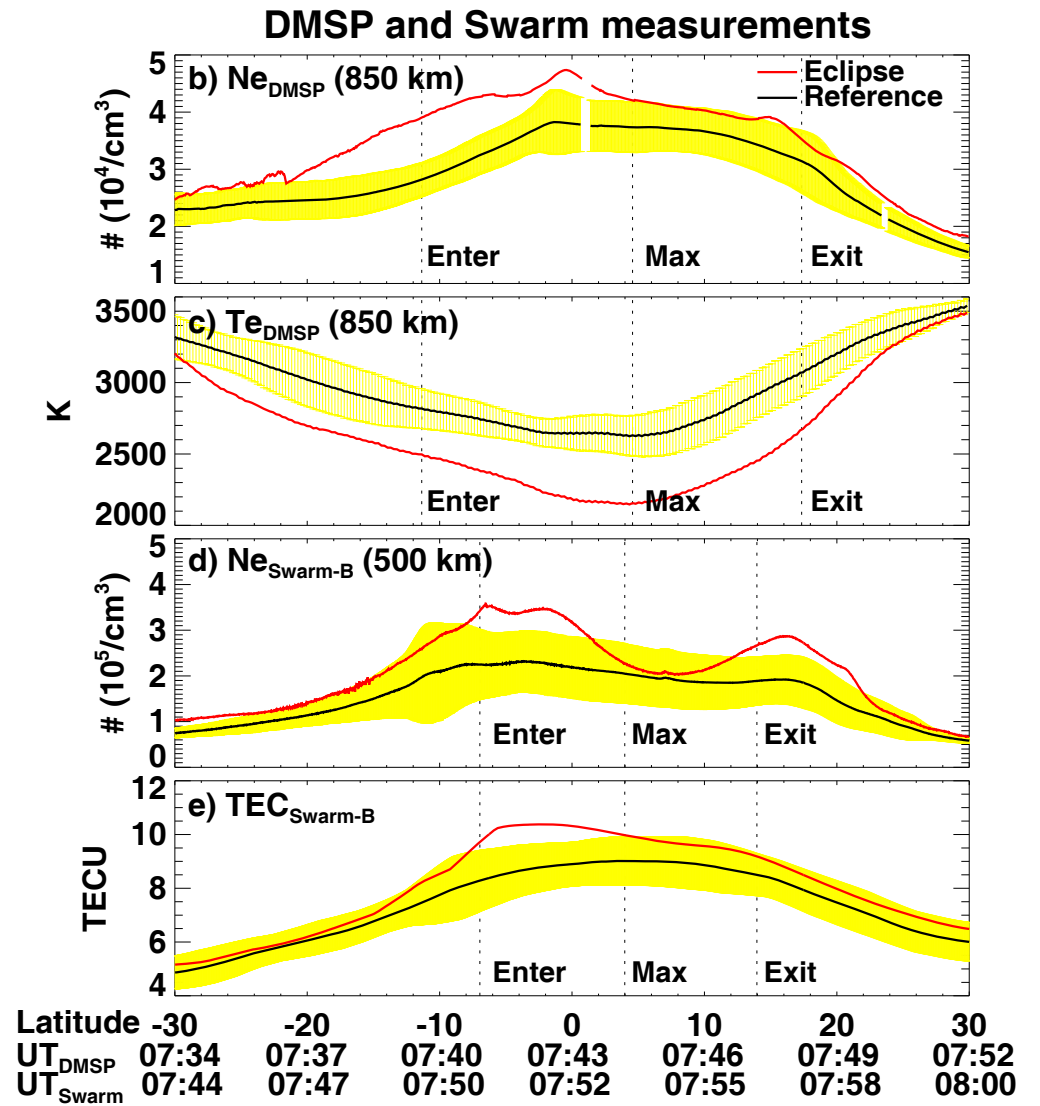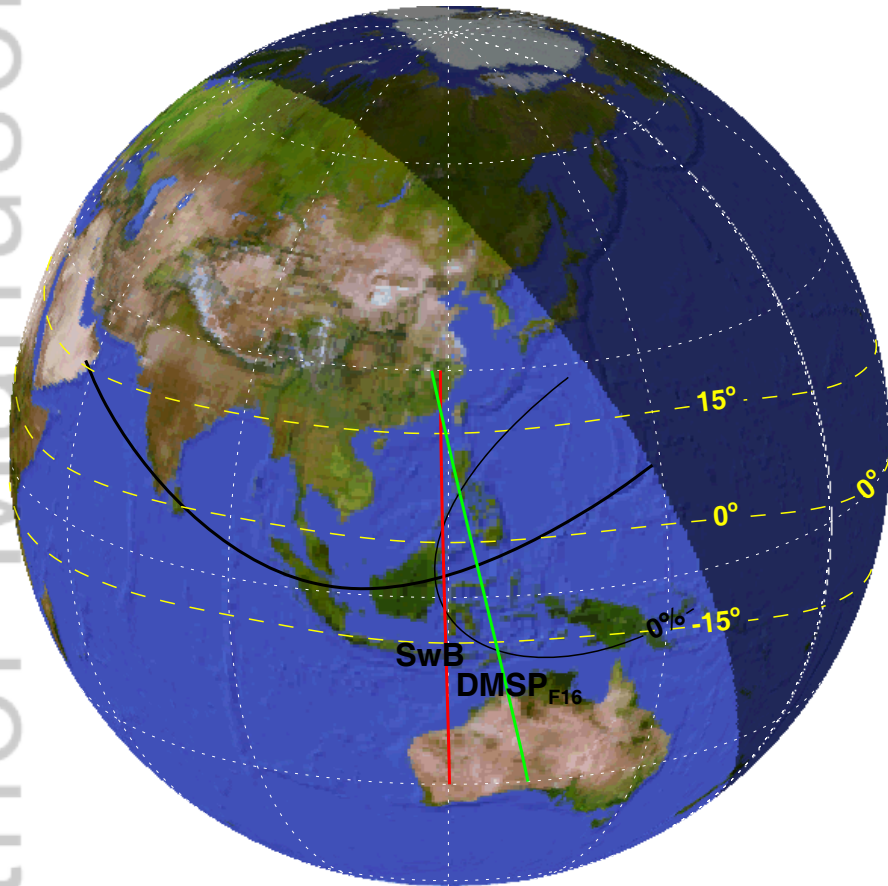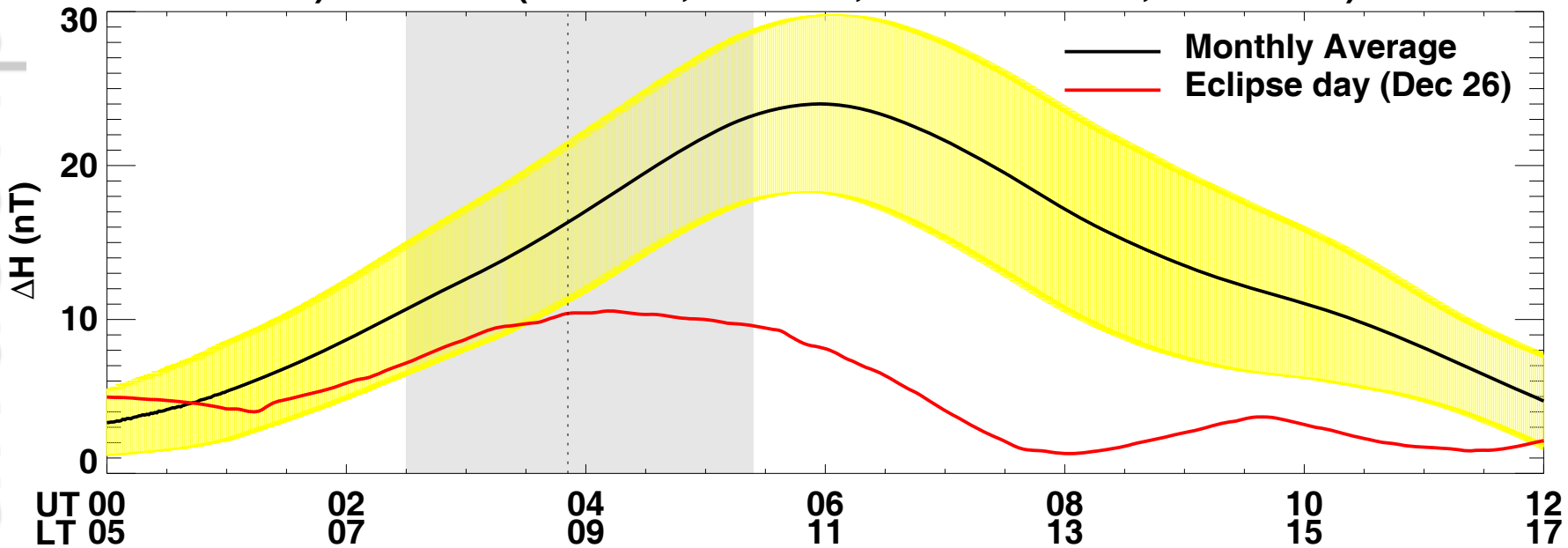| Latitude	-30	-20	-10	0	10	20	30
UT$_{DMSP}$	07:34	07:37	07:40	07:43	07:46	07:49	07:52
UT$_{Swarm}$	07:44	07:47	07:50	07:52	07:55	07:58	08:00

Figure 10.

a) ALIBAG (18.62°N, 72.87°E, MLAT=11.34°, LT=UT+5)

b) Kototabang (0.2°S, 100.32°E, MLAT=−10.03°, LT=UT+7)

Legend:
- Monthly Average
- Eclipse day (Dec 26)